

THE INITIAL CONDITIONS FOR PLANET FORMATION :
TURBULENCE DRIVEN BY HYDRODYNAMICAL INSTABILITIES IN DISKS AROUND YOUNG STARS.

WLADIMIR LYRA^{1,2} AND ORKAN M. UMURHAN^{3,4,★}

(Dated: Received ; Accepted)
Draft version

ABSTRACT

This review examines recent theoretical developments in our understanding of turbulence in cold, non-magnetically active, planetesimal forming regions of protoplanetary disks which we refer to throughout as “Ohmic zones”. We give a brief background introduction to the subject of disk turbulence followed by a terse pedagogical review of the phenomenology of hydrodynamic turbulence. The equations governing the dynamics of cold astrophysical disks are given and basic flow states are described. We discuss the Solberg-Høiland conditions required for stability, and the three recently identified turbulence generating mechanisms possibly active in protoplanetary disk Ohmic zones, namely, (i) the Vertical Shear Instability, (ii) The Convective Overstability and (iii) the Zombie Vortex Instability. We summarize the properties of these processes, identify their limitations and discuss where and under what conditions these processes are active in protoplanetary disk Ohmic zones.

1. INTRODUCTION

Planet formation is simultaneously one of the oldest and one of the newest concerns of human inquiry. “How did the Earth come to be?” is a question that almost invariably appears in the cosmogonies of the ancients. They not always had a clear idea of what “Earth” meant, but this is a question that, in one form or another, virtually every society in recorded history has at some point asked itself. Particularly interesting are the ideas of Leucippus (480-420? B.C.E.) who, according to testimonial, is to have said (Diels & Kranz 1961)

The worlds come into being as follows: many bodies of all sorts and shapes move from the infinite into a great void; they come together there and produce a single whirl, in which, colliding with one another and revolving in all manner of ways, they begin to separate like to like.

Diogenes Laertius IX, 31⁶

This vision strikes surprisingly modern, and not without foundation within the modern theory of planet formation. Substitute “many bodies of all sorts and shapes” by *gas and dust*, then “single whirl” by *protoplanetary disk* and finally “revolving in all manner of ways” by *turbulence*, and it could have figured in the introduction of a paper in the latest issue of a major astronomy journal. This attests not to clairvoyance of the ancient Greeks, but to the antiquity of the question. Given the

huge sample space, some of the educated guesses of the time are bound to contain some truth.

By the 18th century, Newtonian gravity and the orbits of the planets were understood in enough detail to realize that the low inclinations of the orbits implied that the easiest way to attain that configuration was if the planets have formed in a disk that orbited the proto-Sun (Kant 1755). Because Jupiter and Saturn are gas giant planets, this disk must have been a disk of gas. Early mathematical considerations by Laplace (1796) applied Newton’s theory of universal gravitation and laws of motion to a slowly rotating spherical cloud, implying that it should collapse under its own weight. Due to conservation of angular momentum, the gas settles into a flat disk orbiting the condensing proto-Sun in the center. In this *solar nebula*, planets are taking shape.

C. F. von Weizsäcker extended these fundamental notions and pointed out that eddies in the forming solar nebula ought to increase with distance from the Sun prefiguring the role these may have in the formation of planetesimals out of dust (Gamow & Hynke 1945). Rather presciently, Weizsäcker also reasoned that many other star systems should harbor similar kinds of nebulae like our own Sun did after its birth.

Modern searches have now revealed such disks around young stars (Elsasser & Staude 1978; Rucinski 1985; Aumann 1985; Sargent & Beckwith 1987; Strom et al. 1989; Beckwith et al. 1990; O’dell & Wen 1994; McCaughrean & O’dell 1996; Ricci et al. 2008), now called *protoplanetary disks* or, in symmetry with the solar nebula, *extrasolar nebulae* or *exonebulae*. In general, protoplanetary disks range in radius from 10s to 100s of AU (e.g. Ansdell et al. 2018), in density from 10^{13} to 10^{15} cm^{-3} (for mean molecular weight $\mu = 2.5$), in mass from 10^{-3} to $10^{-1} M_{\odot}$, and from 1000 K near the star to 10 K in the outskirts of the disk. These disks form while the star is being formed, as a consequence of the cloud’s gravitational collapse, and here we already find one of the first formidable problems of star and planet formation: as interstellar clouds are huge in size, even the slightest

¹ California State University, Northridge. Department of Physics and Astronomy 18111 Nordhoff St, Northridge, CA 91330, wlyra@csun.edu.

² Jet Propulsion Laboratory, California Institute of Technology, 4800 Oak Grove Drive, Pasadena, CA, 91109, wlyra@jpl.nasa.gov.

³ NASA Ames Research Center, Space Sciences Division, Planetary Sciences Branch, Moffatt Field, CA 94035

⁴ SETI, Carl Sagan Center, 190 Bernardo Way, Mountain View, CA 94043

★ Corresponding Author: orkan.m.umurhan@nasa.gov

⁶ Scholars of the classical period note that nothing but third person accounts survive of Leucippus’ words.

rotation means far too much angular momentum (Mestel 1965a,b). Indeed, if a proto-star was to accommodate all the angular momentum in a ring at 1AU containing about 10% of its mass, it would achieve break-up velocity, a problem that also exists in similar form for the gas giant planets in the Solar System (Takata & Stevenson 1996; Bryan et al. 2018; Batygin 2018). In order to accrete, the gas must somehow find a way to transfer its angular momentum and if a gas parcel does this in nearly circular orbits, it must simultaneously find a way to lose energy in the process.

Because gravity is a radial force, and an axisymmetric disk has no pressure forces in the azimuthal direction, the only process that produces change in angular momentum is viscous stresses. Angular momentum transport is mediated by viscosity; without it, gas will simply orbit the star, not changing its radial position, and star formation will not complete. Although molecular viscosity is much too small to account for the observed mass accretion rate, it was recognized (Shakura & Sunyaev 1973; Lynden-Bell & Pringle 1974) that the stochastic behavior of turbulence would lead to diffusion of momentum, similarly to viscosity. Moreover, while molecular viscosity acts in the small scales of the flow, turbulence acts all the way up to the integral scale, generating much more powerful stresses. The question of angular momentum transport is thus a question of how the disk becomes turbulent.

The 1970s and 1980s saw several possible candidates to generate turbulence and angular momentum transport in disks, such as convection (Cameron 1978; Lin & Papaloizou 1980) or nonlinear instability (Shakura et al. 1978). Yet, it was only with the re-discovery of the magnetorotational instability (MRI; Balbus & Hawley 1991) that the question seemed settled. The MRI entails a combination of a weak (subthermal) magnetic field and the shear present in the Keplerian rotation the gas, that destabilizes the flow. The instability is powerful, seeming to explain the required accretion rates.

The MRI also has a positive effect on planet formation. Starting with micron-sized dust grains, coagulation models (Brauer et al. 2007) predict growth to centimeter size by electromagnetic hit-and-stick mechanisms (mostly van der Waals forces). However, growth beyond this size is halted, for two reasons. First, collisions between pebbles lead to destruction rather than growth (Benz 2000). Second, because of the balance between pressure, rotation and gravity, the gas orbits the star slightly slower than an independent body at the same distance would. Consequently, pebbles tend to outpace the gas. The resulting headwind drains their angular momentum, leading them into spiral trajectories towards the star, in timescales as short as a hundred years at 1AU (Weidenschilling 1977). A distinct possibility to solve these problems is gravitational instability of the layer of solids (Safronov 1972; Lyttleton 1972; Goldreich & Ward 1973; Youdin & Shu 2002). When the dust aggregates had grown to centimeter size, the gas drag is reduced and the solids are pushed to the midplane of the disk due to the stellar gravity. Although such bodies do not have enough mass to attract each other individually, the sedimentation increases the solids-to-gas ratio by orders of magnitude when compared to the interstel-

lar value of 10^{-2} . It was then hypothesized (Safronov 1972) that due to the high densities of this midplane layer, the solids could collectively achieve critical number density and undergo direct gravitational collapse. Such a scenario has the advantage of occurring on very rapid timescales, thus avoiding the radial drift barrier.

This picture was nonetheless shown to be simplistic, in the view that even low levels of turbulence in the disk preclude the midplane layer of solids from achieving densities high enough to trigger the gravitational instability (Weidenschilling 1980). Even in the absence of self-sustained turbulence such as the one generated by the MRI, the solids themselves can generate turbulence due to the backreaction of the drag force onto the gas. Such turbulence can be brought about by Kelvin-Helmholtz instabilities due to the vertical shear the dense layer of solids induces on the gas (Weidenschilling 1980; Weidenschilling & Cuzzi 1993; Sekiya 1998; Johansen et al. 2006), or by streaming instabilities induced by the radial migration of solids particles (Youdin & Goodman 2005; Paardekooper 2006; Youdin & Johansen 2007; Johansen & Youdin 2007). In the turbulent motion, the solids are stirred up by the gas, forming a vertically extended layer where the stellar gravity is balanced by turbulent diffusion (Dubrulle et al. 1995; Garaud & Lin 2004). But if turbulence precludes direct gravitational collapse through sedimentation, it was also shown that it allows for it in an indirect way. As solid particles concentrate in high pressure regions (Haghighipour & Boss 2003), the solids-to-gas ratio can be enhanced in the transient turbulent gas pressure maxima, potentially reaching values high enough to trigger gravitational collapse. Numerical calculations by Johansen et al. (2007) show that this is indeed the case, with the particles trapped in the pressure maxima generated by the MRI collapsing into dwarf planets when the gravitational interaction between particles is considered. While the MRI is not strictly necessary, the streaming instability does not seem to operate effectively for solar and subsolar metallicities, requiring more solids than initially present in the Solar Nebula.

However, the conditions for the magnetorotational instability are not met in a huge portion of the disk (Blaes & Balbus 1994). Being a mechanism that depends on magnetization, it also depends on ionization; as a result, if the ionization fraction is such that resistive effects become important, the MRI may shut down, defining a MRI-dead zone (Blaes & Balbus 1994; Gammie 1996). The partially ionized gas can be seen as a three-fluid system, composed of the ion fluid, the electron fluid, and the neutral fluid. In ideal MHD, where density and ionization fraction are sufficiently high, ions and electrons are tied to the magnetic field and they drag the neutrals along with them; deviations from ideal conditions occur when these fluids start to decouple. In the ambipolar diffusion limit the magnetic field is tied to the electrons and ions, and drifts with them through the neutrals (Blaes & Balbus 1994; Mac Low et al. 1995). In the Ohmic limit collisions with neutrals are efficient in dragging the ions and electrons, and the magnetic field is not frozen in any fluid. In between these limits lies the domain of Hall MHD, where the electrons are coupled to the magnetic field, but collisions with neutrals decouple the ions (Wardle 1999; Balbus & Terquem 2001;

Salmeron & Wardle 2005; Pandey & Wardle 2006; Wardle 2007; Pandey & Wardle 2008; Wardle & Salmeron 2012). At constant magnetic field, this is a progression as density increases, that first the neutrals decouple from magnetic effects (ambipolar diffusion), then the ions (Hall MHD), and finally the electrons (Ohmic resistivity).

We focus on the Ohmic zone, deep into the resistive regime and any magnetic effect is irrelevant. We could have used “hydrodynamical” zone, yet we keep the name Ohmic for juxtaposition to the other non-ideal MHD effects. It is in this non-magnetic regime that the hydrodynamical instabilities we review exist.

The physics of the Hall-dominated and ambipolar-dominated zones is not covered in this review, but we point out their importance in providing boundary conditions for the Ohmic zone. The upper atmosphere of the disk will be dominated by ambipolar diffusion, with the emission of a magnetocentrifugal wind (Bai & Stone 2011; Gressel et al. 2015). As such, it will provide a “lid” to the instabilities here discussed. Until their interaction with the ambipolar zone is defined, we cannot assume that these instabilities are felt in the disk atmosphere; if they are not, they should not be seen in infrared observations. The Hall-dominated zone has a dynamical instability, the Hall shear instability, if the angular momentum vector and the magnetic field are aligned (Kunz 2008; Kunz & Lesur 2013; Lesur et al. 2014; Bai 2015). The reader should keep in mind that our knowledge of the physics of these zones is still taking shape, and it is unclear how the hydrodynamical instabilities we review behave in the ambipolar and Hall zones.

The Ohmic zone is extended. In the inner disk, ionization is provided by thermal collisions. Down to $\approx 900\text{K}$, thermal velocities have enough energy to ionize the alkali metals. This temperature corresponds to a distance of 0.1 AU, depending on the underlying disk model, so only inwards of it will the disk be sufficiently ionized for the MRI. Concurrently, outward of $\approx 30\text{AU}$ (again depending on the underlying disk model), even though the temperatures are low, the column density is low enough that stellar X-rays can ionize the disk throughout. Between these limits, a large dead zone exists. This, incidentally, is squarely where we expect planets to form, at least in the Solar System. If we need turbulence to generate accretion and form planets, we have to look beyond the magnetorotational instability. If star formation necessitates turbulent transport through the accretion disk, and if planet formation needs turbulent pressure maxima to trigger the streaming instability in solar metallicity, we need to look beyond the MRI.

The past few years have seen a number of processes being proposed for purely hydrodynamical instabilities in disks: two linear instabilities, the *Vertical Shear Instability* (Nelson et al. 2013a; Stoll & Kley 2014) and the *Convective Overstability* (Klahr & Hubbard 2014; Lyra 2014), and a non-linear instability the *Zombie Vortex Instability* (Marcus et al. 2015, 2016). These processes were linked to different regimes of opacities by Malygin et al. (2017). It is the purpose of this review to frame these disparate processes into a coherent picture of hydrodynamical processes in Ohmic dead zones of accretion disks. This review is organized as follows. In the next section we briefly review the physics of accretion disks. On Sect. 3

we give an overview of turbulence, introducing the hydrodynamical instabilities on Sect. 4. A synthesis, the main goal of this review, is given on Sect. 5. Following it, Sect. 6 presents our opinion for the directions of the field in the next few years, finally concluding on Sect. 7.

2. ASTROPHYSICAL DISKS: EQUATIONS AND STEADY STATES

Disks are objects in steady state. They are gaseous objects, so we need to solve the equations of hydrodynamics in a central potential. The equations to solve are

$$\frac{\partial \rho}{\partial t} = -(\mathbf{u} \cdot \nabla) \rho - \rho \nabla \cdot \mathbf{u}, \quad (1)$$

$$\rho \frac{\partial \mathbf{u}}{\partial t} = -\rho (\mathbf{u} \cdot \nabla) \mathbf{u} - \nabla p - \rho \nabla \Phi + \nabla \cdot \mathbf{T} + \mathbf{F}, \quad (2)$$

$$p = \rho c_s^2 / \gamma \quad (3)$$

$$\Phi = -\frac{GM_\star}{r}, \quad (4)$$

where ρ is density, \mathbf{u} is the velocity, p is the pressure (assumed to be that of an ideal gas law), Φ is the gravitational potential, c_s is the sound speed in which $c_s^2 \equiv \gamma RT / \mu$ where T is the gas temperature, μ the gas mean molecular weight, R is universal gas constant, and γ is the adiabatic index given by the ratio of specific heats at constant pressure and volume respectively. Additional body forces are represented by the vector \mathbf{F} . Finally, G is the gravitational constant, M_\star is the stellar mass, and r the astrocentric distance. The mathematical symbols used in this work are listed in Table 1.

The symmetric viscous stress tensor is \mathbf{T} , and in Cartesian coordinates it is expressed according to the Einstein index convention form

$$\mathbf{T} \leftrightarrow T_{ik} \equiv \zeta \left[\left(\frac{\partial u_i}{\partial x_k} + \frac{\partial u_k}{\partial x_i} \right) - \frac{2}{3} \delta_{ik} \frac{\partial u_m}{\partial x_m} \right] + \zeta \delta_{ik} \frac{\partial u_m}{\partial x_m}, \quad (5)$$

and recalling that according to this convention, repeated indices are summed over from 1 to 3. Thus,

$$\nabla \cdot \mathbf{T} \leftrightarrow \frac{\partial T_{ik}}{\partial x_k} = \frac{\partial T_{i1}}{\partial x_1} + \frac{\partial T_{i2}}{\partial x_2} + \frac{\partial T_{i3}}{\partial x_3}. \quad (6)$$

The quantities ζ and ζ are the dynamic shear and bulk *molecular* viscosities whose values are rooted in the mean free paths of the molecules of the gas (e.g., of molecular hydrogen). From a topological point of view, there are two kinds of material motions, either purely compressive or purely incompressible. Each type of motion will have different properties with respect to the transfer or momentum at the molecular level wherein compressible motions will have a corresponding bulk viscosity while incompressible motions will have a corresponding shear viscosity. Since most motions of interest for disks have a primarily incompressible character it is usual practice to ignore the bulk viscosity. As such, then we may define a viscous diffusion $\nu \equiv \zeta / \rho$. If further \mathcal{U} and \mathcal{L} respectively represent scales typifying unsteady flow speeds and length scales of the fluid system, then one can characterise the relative importance of viscosity through the definition of the Reynolds number

$$\text{Re} \equiv \mathcal{U} \mathcal{L} / \nu. \quad (7)$$

TABLE 1
 SYMBOLS USED IN THIS WORK.

Symbol	Definition	Description	Symbol	Definition	Description
R		cylindrical radial coordinate	N_z	Eq. (80)	vertical Brunt-Väisälä frequency
ϕ		azimuth	N_R	Eq. (79)	radial Brunt-Väisälä frequency
z		vertical coordinate	\mathbf{F}		body force
r		spherical radial coordinate	ℓ	$\approx 2\pi/k$	vortex eddy length scale
λ		wavelength	u_ℓ		typical eddy speed
k	$= 2\pi/\lambda$	wavenumber	t_ℓ	$\approx \ell/u_\ell$	eddy overturn time
m		azimuthal wavenumber	ℓ_0		energy injection scale
t		time	ℓ_{diss}		dissipation length scale
ρ		density	ε	$\text{erg s}^{-1} \text{g}^{-1}$	energy dissipation rate per unit mass
\mathbf{u}		velocity	E_k		energy per mass in eddies between k and $k + \delta k$
T		temperature	\mathcal{E}	$= E_k/k$	energy per mass density
γ		adiabatic index	$\boldsymbol{\omega}$	$= \nabla \times \mathbf{u}$	vorticity
c_p		specific heat at constant pressure	\mathcal{Z}	$= \boldsymbol{\omega}^2$	enstrophy
c_v	$= c_p/\gamma$	specific heat at constant volume	Ψ	$\mathbf{u} = \nabla \times \Psi \hat{\mathbf{z}}$	streamfunction
c_s	$= [T c_p(\gamma-1)]^{1/2}$	sound speed	Ω_{PV}	$= \rho^{-1} \boldsymbol{\omega} \cdot \nabla s$	potential vorticity
p	$= c_v(\gamma-1)\rho T$	pressure	β_{PV}	$\equiv \frac{\partial \Omega_{\text{PV}}}{\partial q}$	potential vorticity gradient
s	$= c_v \ln(p/\rho^\gamma)$	specific entropy	l		latitude
Φ	$= -GM_\star/r$	gravitational potential	Ω_{GPV}	Eq. (127)	generalized potential vorticity
G		gravitational constant	$u'_i u'_j$		spatial correlation of component velocity fluctuations
M_\star		stellar mass	σ_{SB}		Stefan-Boltzmann constant
μ		mean molecular weight	α	$= \overline{u'_r u'_\phi} / c_s^2$	measure of turbulent intensity
R		gas constant	ν_t	$= \alpha c_s H$	effective turbulent viscosity
\mathbf{T}		viscous stress tensor	L	$= R^2 \Omega$	angular momentum
ζ		dynamic shear molecular viscosity	K		spring constant
$\tilde{\zeta}$		dynamic bulk molecular viscosity	q		generalized coordinate
ν	$= \zeta/\rho$	kinematic viscosity	ξ		Lagrangian displacement
Re	$= \mathcal{U} \mathcal{L} / \nu$	Reynolds number	\mathbf{B}		magnetic field
\mathcal{U}		representative velocity	v_A	$= B / \sqrt{4\pi\rho}$	Alfvén velocity
\mathcal{L}		representative length	β	$= 2c_s^2 / v_A^2$	plasma beta
Q		heat source	η		resistivity
Ω	$= \sqrt{GM_\star/R^3}$	Keplerian angular frequency	\mathbf{J}		current
H	$= c_s / \Omega$	disk scale height	c		speed of light
h	$= H/R$	disk aspect ratio	Re_M	$= \mathcal{U} \mathcal{L} / \eta$	Magnetic Reynolds number
Σ	$\propto \rho H$	column density	Λ	$= v_A^2 / \Omega \eta$	Elssasser number
q	$= -d \ln \Omega / d \ln R$	shear parameter	Z		charge multiplicity
q_ρ	$= -d \ln \rho / d \ln R$	radial density gradient	γ_i	$\mathbf{f} \equiv \gamma_i \rho_i \rho (\mathbf{u}_i - \mathbf{u})$	ion-neutral drag coefficient
q_T	$= -d \ln T / d \ln R$	radial temperature gradient	σ_{coll}		collisional cross section
q_Σ	$= -d \ln \Sigma / d \ln r$	column density gradient	n		number density
ω		complex eigenfrequency	x	$\equiv n_e / n$	ionization fraction
σ	$= \text{Im}(\tilde{\omega})$	growth rate	κ_R		Rossland mean opacity
Ma	$= \mathcal{U} / c_s$	Mach number	ℓ_r	$= (\kappa_r \rho)^{-1}$	photon mean free path
κ_{ep}	$= \Omega \sqrt{2(2-q)}$	epicyclic frequency	τ_r	Eq. (129)	thermal relaxation time
\mathcal{A}_k	$= c_s \partial_k \ln \rho$	normalized density gradient	a_{rad}	$= 4\sigma_{\text{SB}} / c$	Radiation constant
\mathcal{G}_k	$= \gamma^{-1} c_s \partial_k \ln p$	normalized pressure gradient	χ		Coefficient of thermal diffusion
\mathcal{S}_k	$= \mathcal{G}_k - \mathcal{A}_k$	normalized entropy gradient	Ro		Rosby number

A very large value of Re indicates that viscosity is relatively weak. For protoplanetary disks, values of Re can be as high as 10^{14} which is based on (i) the values of H_2 's viscosity, (ii) the assumption that local sound-speeds give an upper limit of the fluctuating velocity scales and, (iii) the local disk pressure scale height describes relevant length scales. In practice then, owing to the small values of these viscosities and the large scales of interest, protoplanetary disk flows are treated as being inviscid and these stress terms are dropped. However we will eventually come full-circle: owing to the strong linear instabilities found in these flows, we must

replace these stress terms with an equivalent *turbulent* viscosity model in order to account for the flow of turbulent energy (see discussion in Sect. 3).

Lastly, these equations must be supplemented with one describing the energy/entropy content of the flow. Typically, we start with the evolution equation for the entropy,

$$\rho T \left(\frac{\partial s}{\partial t} + \mathbf{u} \cdot \nabla s \right) = Q. \quad (8)$$

where the specific entropy s is defined based on the specific heat at constant volume

$$s \equiv c_v \ln(p/\rho^\gamma). \quad (9)$$

The heat source term \mathcal{Q} will usually have a viscous heating and either a radiative cooling or thermal diffusion term. For locally isothermal disks, one simply sets $\gamma = 1$ in Eq. (3) and not solve Eq. (8).

Writing Eq. (1) and Eq. (2) in cylindrical coordinates (R, ϕ, z) we find, without the viscous terms

$$\frac{\partial \rho}{\partial t} = -u_R \frac{\partial \rho}{\partial R} - \frac{u_\phi}{R} \frac{\partial \rho}{\partial \phi} - u_z \frac{\partial \rho}{\partial z} - \rho \left(\frac{\partial u_R}{\partial R} + \frac{u_R}{R} + \frac{1}{R} \frac{\partial u_\phi}{\partial \phi} + \frac{\partial u_z}{\partial z} \right) \quad (10)$$

$$\frac{\partial u_R}{\partial t} = -u_R \frac{\partial u_R}{\partial R} - \frac{u_\phi}{R} \frac{\partial u_R}{\partial \phi} - u_z \frac{\partial u_R}{\partial z} + \frac{u_\phi^2}{R} - \frac{1}{\rho} \frac{\partial p}{\partial R} - \frac{GM}{r^3} R \quad (11)$$

$$\frac{\partial u_\phi}{\partial t} = -u_R \frac{\partial u_\phi}{\partial R} - \frac{u_\phi}{R} \frac{\partial u_\phi}{\partial \phi} - u_z \frac{\partial u_\phi}{\partial z} - \frac{u_\phi u_R}{R} - \frac{1}{\rho R} \frac{\partial p}{\partial \phi} \quad (12)$$

$$\frac{\partial u_z}{\partial t} = -u_R \frac{\partial u_z}{\partial R} - \frac{u_\phi}{R} \frac{\partial u_z}{\partial \phi} - u_z \frac{\partial u_z}{\partial z} - \frac{1}{\rho} \frac{\partial p}{\partial z} - \frac{GM}{r^3} z \quad (13)$$

We look for steady state solutions, so $\partial_t = 0$. We also assume azimuthal symmetry, setting $\partial_\phi = 0$. Consider also that the disk is in vertical hydrostatic equilibrium, so $u_z = 0$. Plus, for the moment we assume that the centrifugal balance is maintained, so $u_r = 0$. With these constraints, the continuity and angular momentum equations admit only the trivial solution, and we are left with quite little

$$\frac{GM}{r^3} R = -\frac{1}{\rho} \frac{\partial p}{\partial R} + \Omega^2 R, \quad (14)$$

$$\frac{GM}{r^3} z = -\frac{1}{\rho} \frac{\partial p}{\partial z}. \quad (15)$$

The first equation above is what is left of the radial momentum equation, and the second one from the vertical momentum equation. These equations highlight why disks are flat. It is the influence of the centrifugal force: while pressure counterbalancing gravity makes things spherical, the centrifugal force makes things cylindrical. The relative strength of the pressure and the centrifugal terms defines if the object will appear more on the spherical side, in hydrostatic equilibrium, or more on the flat side, in centrifugal steady state. A pressure-supported object is spherical, whereas a centrifugally-supported object is flat. Eq. (15) gives the condition of vertical hydrostatic equilibrium, which we turn to now.

2.1. Vertical hydrostatic equilibrium

If we assume an isothermal equation of state, or simply that the sound speed does not depend on z , so we can write $c_s = c_s(R)$, we can solve for the vertical structure

$$\frac{\partial \ln \rho}{\partial z} = -\frac{GM}{c_s^2} \frac{z}{r^3} \quad (16)$$

which is integrated to yield

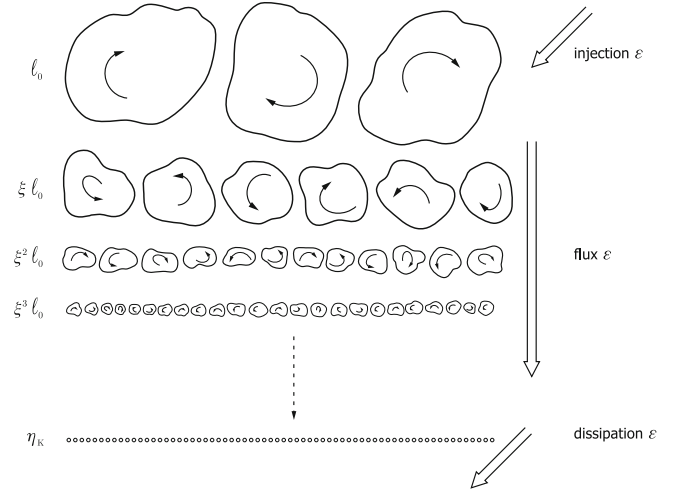


FIG. 1.— A cartoon image of turbulent cascade as cast into verse by L.F. Richardson (1881-1953) “*Big whirls have little whirls/That feed on their velocity,/And little whirls have lesser whirls/And so on to viscosity.*” Each daughter generation is scaled by its parent size by ζ . η_K is the same as the dissipation scale ℓ_{diss} , sometimes also known as the Kolmogorov microscale. Throughout this inertial range, there is no build up of power – only a flux of ϵ shuttling energy from larger to smaller scales via nonlinear interactions. [Figure from Regev et al. (2016), by permission.]

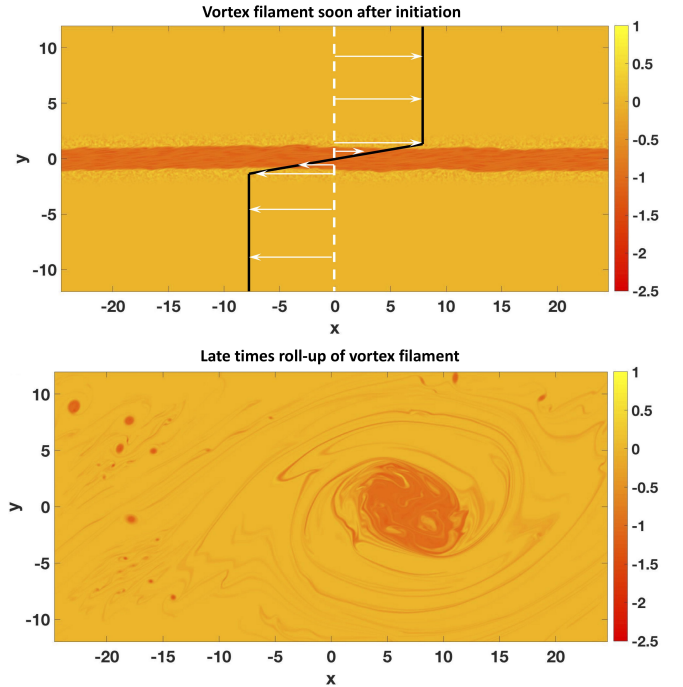


FIG. 2.— Roll-up of 2D vortex strip. Top panel shows vortex strip (shear layer) soon after initiation with vorticity shown in side intensity panel. Overlain is the sense of the mean velocity field $u(y)$. Bottom panel shows the result of the roll-up of this shear layer. The final resulting structure is larger in scale compared to the initial shear layer indicating an inverse cascade of energy. However, the roll-up has also generated small scale vortex filaments – indicating the generation of vorticity on scales much smaller than the original strip. [Figure adapted from Biancofiore & Umurhan (2018), by permission.]

$$\rho(R, z) = \rho(R) \exp \left[\frac{GM}{c_s^2} \left(\frac{1}{\sqrt{R^2 + z^2}} - \frac{1}{R} \right) \right]. \quad (17)$$

We can write $\sqrt{R^2 + z^2} = R\sqrt{1 + (z/R)^2}$, and expand in Taylor series to first order to find

$$\rho(R, z) = \rho(R) \exp \left(-\frac{GM}{2c_s^2 R^3} z^2 \right). \quad (18)$$

The quantity $c_s^2 R^3 / GM$ has dimension of length (squared) and thus defines a scale height. GM/R^3 is the square of the Keplerian angular frequency

$$\Omega_K \equiv \sqrt{\frac{GM}{R^3}} \quad (19)$$

So

$$H \equiv \frac{c_s}{\Omega_K}, \quad (20)$$

and we can write the density stratification compactly

$$\rho(R, z) = \rho(R) e^{-\frac{z^2}{2H^2}}. \quad (21)$$

Note that $c_s = \Omega_K H$ and $u_K = \Omega_K R$, so

$$\frac{H}{R} = \frac{c_s}{u_K} \equiv \frac{1}{\text{Ma}} \quad (22)$$

At the position of Jupiter, $T \approx 180\text{K}$ and $u_K \approx 10\text{ km/s}$, so $c_s \approx 500\text{ m/s}$ and thus $H/R \approx 0.05$, rendering the disk thin. This quantity, $h \equiv H/R$, is usually called the disk aspect ratio. Another feature to notice is that given $\Omega \sim R^{-3/2}$, and if temperature dependence is described by $T \sim R^{-q_T}$, where q_T is an index (see below), then for values of $q_T < 3/2$ we see that the scale height H increases with distance. For $q_T = 1$ it follows that the aspect ratio $h = H/R$ is constant.

2.2. Radial Centrifugal balance

Having solved for the disk vertical structure, we turn to the radial equation, Eq. (14). We can write the pressure gradient as

$$\frac{1}{\rho} \frac{\partial p}{\partial R} = c_s^2 \left[\frac{\partial \ln \rho}{\partial R} + \frac{\partial \ln c_s^2}{\partial R} \right] \quad (23)$$

and given the hydrostatic solution for density, Eq. (17)

$$\frac{1}{\rho} \frac{\partial p}{\partial R} = -\frac{c_s^2}{R} (q_\rho + q_T) + \frac{GM}{R^2} - \frac{GM}{r^3} R - \frac{GM}{R^3} z^2 \frac{q_T}{2R} \quad (24)$$

where we also assumed radial power laws for density and temperature

$$\rho(R) \propto R^{-q_\rho}, \quad (25)$$

$$T(R) \propto R^{-q_T}. \quad (26)$$

Substituting the pressure gradient on Eq. (14) and solving for Ω

$$\Omega^2 = \frac{GM}{R^3} - \frac{c_s^2}{R^2} (q_\rho + q_T) - \frac{GM}{R^3} z^2 \frac{q_T}{2R}. \quad (27)$$

Finally, substituting the definition of Ω_K , we find

$$\Omega = \Omega_K \left\{ 1 - \frac{1}{2} \left(\frac{H}{R} \right)^2 \left[q_\rho + q_T + \frac{q_T}{2} \left(\frac{z}{H} \right)^2 \right] \right\} \quad (28)$$

Notice that if $q_\rho = q_T = 0$, i.e., no pressure gradient, the angular frequency returns to Keplerian. Also, because H/R is small, the deviations from Keplerian are also small.

Before we address how this steady-state configuration transitions via linear and nonlinear instabilities into full-blown protoplanetary disk turbulence, we must give a brief overview of how turbulence is confronted in this astrophysical context.

2.3. Ertel's theorem and Rossby Waves

A theorem and quantity of singular importance emerges from an analysis of the equations of motion. If we assume both no heat gain or losses in the flow ($Q = 0$, which means that the gas specific entropy s is materially conserved), and we neglect gas viscosity by setting $\mathbf{T} = 0$, then a manipulation of the resulting equations of motion reveals a conserved quantity

$$\left(\frac{\partial}{\partial t} + \mathbf{u} \cdot \nabla \right) \frac{\boldsymbol{\varpi} \cdot \nabla s}{\rho} = 0, \quad (29)$$

where $\boldsymbol{\varpi} \equiv \nabla \times \mathbf{u}$ is the vorticity. The conserved quantity is called *potential vorticity*

$$\Omega_{\text{PV}} \equiv \frac{\boldsymbol{\varpi} \cdot \nabla s}{\rho}, \quad (30)$$

and Eq. (29) is known as Ertel's theorem; a succinct derivation may be found in Regev et al. (2016). The dynamical importance of the conservation of potential vorticity (often known as "PV") and its use as a tool to interpret flows – especially those that are strongly rotating and/or ones with one spatial dimension severely limited like in planetary atmospheres and disks – cannot be overstated (Pedlosky 1982).

While a thorough survey of its consequences is not possible here (for a good introductory view see Vallis 2006), it is important to discuss a dynamical phenomenon that emerges as a consequence of perturbations of Eq. (29), namely, the ubiquity of the *Rossby wave*. To best illustrate the Rossby wave, we consider a very shallow constant density fluid layer on a rotating sphere with constant radially directed gravity. If the rotation vector of the spinning sphere of radius R_0 is $\Omega \hat{\mathbf{z}}$, where $\hat{\mathbf{z}}$ is the spin axis and the constant $\Omega_0 > 0$, and if the fluid layer depth is H (and constant for our purpose), then the entropy gradient is a delta function with radial unit vector $\hat{\mathbf{r}}$. Since for a given observer at latitude l , the inner product $\hat{\mathbf{r}} \cdot \hat{\mathbf{z}} = \cos l$, it follows that Ω_{PV} is non-zero at the location of the entropy gradient which is taken to be the surface of the sphere for the sake of simplicity. The PV then has the form $2\Omega \cos l$. It can be seen that global PV increases with increasing latitude. Introduction of perturbations to an otherwise static rotating

atmosphere will result in a wave response known as the Rossby wave. To see this consider a small latitudinal zone centered at some given latitude l_0 . If we expand Ω_{PV}

$$= 2\Omega_0 + \beta_{\text{PV}}(y - y_0), \quad (31)$$

where

$$2\Omega_0 = 2\Omega \cos l_0 \quad \beta_{\text{PV}} \equiv \left. \frac{1}{R} \frac{\partial \Omega_{\text{PV}}}{\partial l} \right|_{l=l_0}, \quad (32)$$

in which y has units of length, then we can perform an approximate linear perturbation analysis of Eq. (29) assuming strictly two-dimensional incompressible flow whose details can be found in Pedlosky (1982). Perturbations of the form $\exp(i\omega t + ik_x x + ik_y y)$ in which ω is the frequency response, x is the longitudinal distance and where k_x and k_y are the corresponding wavevector of the disturbance results in a Rossby wave frequency response given by

$$\omega_{\text{RW}} = \frac{\beta_{\text{PV}} k_x}{k_x^2 + k_y^2}. \quad (33)$$

We might imagine a circumplanetary level-set of constant PV being perturbed with a wavelength k_x and k_y . The frequency response indicates that the longitudinal wave pattern propagates in the negative longitudinal (westerly) direction. This is a general feature of systems supporting Rossby waves: in a right-handed coordinate system, positive latitudinal gradients in PV results in a negative pattern speed of the resulting wave.

Rossby waves are also prevalent in protoplanetary disks and this has been extensively written about (Lovelace et al. 1999; Li et al. 2000; Umurhan 2010). There are notable differences, the main one being: while accretion disks exhibit gradients in their mean PV simply owing to the mean Keplerian flow, Rossby waves are mostly supported where there are anomalous changes in the mean Keplerian flow, like locations where the disk material supports pressure extrema (Lovelace et al. 1999; Li et al. 2000; Meheut et al. 2010; Lin 2014) or where there are sharp edges like near disk gaps (Koller et al. 2003; de Val-Borro et al. 2007; Lyra et al. 2009; Yellin-Bergovoy et al. 2017), or potentially in places where the disk goes from being Ohmic to significantly magnetized (Varnière & Tagger 2006; Lyra & Mac Low 2012). However, the Rossby wave frequency response estimated based on our simplified rotating sphere model, Eq. (33), may be also a useful guide for disks as well (Sheehan et al. 1999). At a local radial position R_0 in a Keplerian disk with rotation $\Omega = \Omega_0(R_0/R)^{3/2}$, in which the disk material moves only in the azimuthal-radial directions and the fluid is idealized to be of constant density of finite disk thickness, then we find that

$$\Omega_{\text{PV}} = \frac{1}{R} \frac{\partial(\Omega R)}{\partial R} = \frac{\Omega}{2}, \quad (34)$$

and following Sheehan et al. (1999), adopting the same line of thinking we can estimate the β_{PV} -parameter to be

$$\beta_{\text{PV}} \sim \left. \frac{\partial \Omega_{\text{PV}}}{\partial R} \right|_{R=R_0} = -\frac{3}{4} \frac{\Omega}{R}. \quad (35)$$

3. TURBULENCE: A TERSE OVERVIEW.

Fluid turbulence remains one of last unsolved problems of classical physics (Davidson 2004) and despite over 100 years of research by thousands of scientists and engineers, very little can be said. Many who work in the field, when asked “*What is turbulence?*”, respond with “*I do not really know, but I know it when I see it.*” Fluid flows that undergo turbulent transition can be said to display widespread structural disorder and chaos. They are inherently unpredictable and highly nonlinear. Unstable fluid structures in the grips of turbulence can completely fill up the totality of the fluid volume containing the turbulence (like what happens in the bounded regions containing unstable jet flows or wakes) or display sublimity like spatiotemporal intermittency, i.e., regions and pockets in space and/or time where the flow exhibits laminar behavior surrounded by regions of high intensity vortex tube twisting and attendant chaos.

There are several possible routes to turbulence in any fluid setting. In the context of protoplanetary disk Ohmic zones, we focus on the picture of *supercritical transition* wherein the system of interest, generally in some steady state, will experience a linear instability if physical conditions in the fluid are met – we refer to this as the *primary instability*. If the physical criteria controlling the onset are only weakly surpassed by the physical state of the fluid system, then often times the flow will reconfigure itself into some new nonlinear state – often time-dependent with an identifiable set of periods – but nevertheless orderly structured and predictable. If the physical conditions greatly surpass the criterion for onset, then even this nonlinear state may experience an instability and when this happens we refer to it as the *secondary instability*. This transition might result in another, even more complicated, nonlinear state to emerge – or – this transition could lead to a catastrophic cascade and a complete breakdown of any ordered flow structure.

Of many consequences of such chaotic situations, an important one is that fluid vortical structures emerging on every scale will vigorously exchange angular momentum with one another. Another feature to keep in mind is that every time a transition occurs in the flow, the system generally loses some symmetry it once possessed before the instability. A fully turbulent state has lost all semblance of symmetries that are permissible in the governing equations of motion. Ironically, these lost symmetries return when the flow is viewed from a statistical and/or spatiotemporally averaged point of view.

For example, in dissipative MRI turbulence the primary instability leads to the emergence of a radial component to the basic Keplerian state which periodically reverses sign as a function of distance away from the disk midplane. Because of the emergence of a strong vertical shear in this radial velocity component, the new flow state undergoes a secondary instability via the excitation of parasitic instabilities (Goodman & Xu 1994) which is an element of the wider class of shear instabilities. This result is a dynamical cascade into widespread and very strong turbulence that effectively transports angular momentum.

From this general perspective and for our purposes here we assume that (i) there is a continuous energy

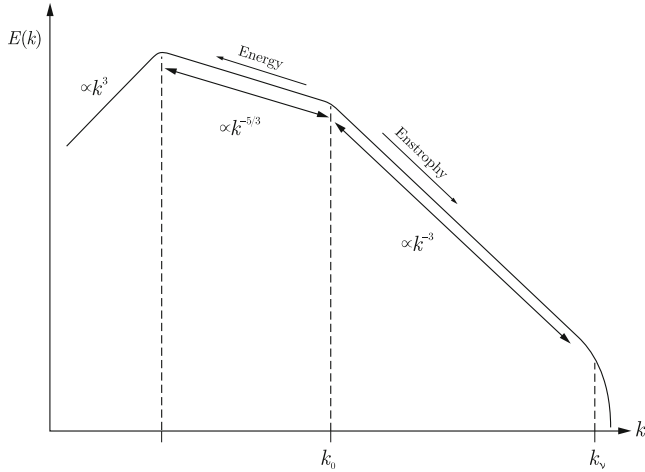


FIG. 3.— The double cascade spectrum of the Kraichnan-Batchelor theory of 2D steady driven turbulence. The injection scale is $k_0 = 2\pi/\ell_0$. The two cascade regimes are indicated. The inclusion of linear dissipation acting only at the largest scales accounts for the k^3 character of the energy spectrum in that regime. Simulations of Boffetta & Musacchio (2010) largely bear out the character of this theory. [Figure from Regev et al. (2016), by permission.]

source for the turbulence, (ii) it enters the system at some integral scale of the system ℓ_0 and, (iii) it steadily injects energy on these scales at a given rate, ε – a quantity typically expressed in units of energy per unit time per unit mass ($\text{erg s}^{-1} \text{g}^{-1}$, or cm^2/s^3).

From the vantage point of astrophysical flows like protoplanetary disks, the presence or absence of turbulence has several profound effects. Of importance to us (and as intimated above) is the ability of turbulent structures to transport angular momentum. In regions centered on the midplane at 5AU in a disk surrounding a 1 solar mass star, the Reynolds number $\text{Re} = \mathcal{U}\mathcal{L}/\nu$ with velocities \mathcal{U} of the order of the sound speed and length \mathcal{L} of the order of the local scale height H is roughly 10^{13-14} , based on molecular hydrogen’s viscous diffusivity $\nu \sim 10^3 \text{cm}^2 \text{s}^{-1}$. The corresponding viscous dissipation scale (Regev et al. 2016) is $\ell_{\text{diss}} \sim \text{Re}^{-3/4}H \approx 0.1 - 1 \text{km}$. This means that the character of the unsteady flow between the scales that drive the turbulence from the generation scales (an order unity fraction of H) down to the dissipation scale ℓ_{diss} must somehow be characterized. Currently, only a crude mixing-length theory characterization exists for disks (see Sect. 3.5).

3.1. Kinetic energy spectra

Flows which exhibit turbulence can be identified (at least in part) by their statistical properties. The flow is presumed to have a mean state plus a spatiotemporally fluctuating field, respectively given by $\bar{\mathbf{u}}$ and \mathbf{u}' . In most instances, one examines the kinetic energy contained in fluctuating quantities by constructing its *energy spectrum*. This is most readily seen if we assume \mathbf{u}' to be periodic in each spatial dimension. Provided the dimensions containing the fluid, \mathcal{L} , is sufficiently larger than the injection scales, then we can identify all components of the fluctuating field exhibiting spatial structure with absolute value of the wavenumber $|\mathbf{k}| = k \equiv 2\pi/\ell$,

where ℓ is the spatial scale of the fluctuating quantity. Let us define E_k as being the total specific energy in the flow contained in fluid structures whose wavenumber lies between k and $k + \delta k$. The specific energy is understood to be the energy per unit mass (cm^2/s^2) – for the purposes of discussion we assume the flow has constant density and we will consider the corresponding specific kinetic energy. The *power* in this specific energy is formally defined through the relationship expressing the total specific energy contained in the fluctuating flow field whose wavenumbers lie between k and $k + \delta k$, i.e.,

$$E_k = \mathcal{E}(k)\delta k \equiv \int_k^{k+\delta k} \mathcal{E} dk, \quad \lim_{\delta k \rightarrow 0} \mathcal{E}(k) \rightarrow \frac{\partial E_k}{\partial k}. \quad (36)$$

$\mathcal{E}(k)$ has units of cm^3/s^2 . Evidently, the system integrated total specific energy, E , is the integral of \mathcal{E} over all wavenumbers, i.e.,

$$E = \int_0^\infty \mathcal{E} dk. \quad (37)$$

When E_k behaves as a power law (at least locally in k), a quick estimate for \mathcal{E} is $\approx E_k/k$.

$\mathcal{E}(k)$ is a diagnostic quantity reflecting the state of the fluid at any given instant. If the turbulence is in a statistically steady state – where injected power is ultimately drained from the system through either by molecular viscosity on the smallest scales, or by Ekman pumping and/or radiative losses to space on the largest scales – then $\mathcal{E}(k)$ will be steady over some suitable time average. Because fluid systems like the Navier-Stokes equations are highly nonlinear, energy contained in one narrow band of wavenumbers can be traded to other fluid structures of differing wavenumber through the process of nonlinear interactions. Sometimes the energy exchange is local in wavenumber space, but other times the exchange can occur between structures of vastly differing length scales.

3.2. 3D isotropic turbulence: Kolmogorov-Obukhov theory and Richardson cascade

What little that can be said about freely evolving turbulence of the 3D incompressible Navier-Stokes equations relate to its observed statistical properties expressed as some signature quality of $\mathcal{E}(k)$. The Kolmogorov-Obukhov theory of 3D isotropic turbulence offers an explanation predicated on certain assumptions about the flow, namely that it is (i) homogeneous and isotropic, (ii) self-similar and, (iii) the dissipation rate is constant. A detailed discussion about this theory can be found in Davidson (2004). We offer a crude sketch to convey the essence of the theory as describing statistically steady state turbulence. The notion that the fully developed state is homogeneous and isotropic is to be understood from this time-averaged statistical point of view.

In this light we consider what happens to structures whose size ℓ is much smaller than the injection scale ℓ_0 but much larger than the dissipation scales ℓ_{diss} . We call this size range the *inertial regime*. Thus, the first two of these assumptions give rise to the so-called Richardson cascade (see Fig. 1) governing what happens in the inertial regime, in which a given 3D twisting vortex of

some size ℓ , with rotation speed u_ℓ , undergoes a nonlinear bifurcation that generates smaller-sized (scaled on ℓ by $0 < \xi < 1$) daughter 3D vortex structures, also see discussion also found in Frisch (1995). We can think of the vortical structure on scale ℓ as "living" only for one rotation time before undergoing "destruction", i.e., $t_\ell = \ell/u_\ell$. In this steady state picture, the rate of energy entering and exiting every length scale must be the same, i.e., ε is independent of ℓ . Thus, we say that this energy rate is given by its energy divided by this rotation time. In terms of the specific energy this means to say,

$$\varepsilon = \frac{u_\ell^2/2}{t_\ell} \sim \frac{u_\ell^3}{\ell}, \rightarrow u_\ell \sim (\varepsilon \ell)^{-1/3} \sim \varepsilon^{1/3} k^{-1/3}. \quad (38)$$

It immediately follows that the energy contained on the length scale ℓ

$$E_k = u_\ell^2/2 \sim \varepsilon^{2/3} k^{-2/3}. \quad (39)$$

This is sometimes known as the Kolmogorov two-thirds rule. The amount of power in the small wavelength bin containing k is therefore expressed by $\mathcal{E} \approx E_k/k \sim \varepsilon^{2/3} k^{-5/3}$. This is the famous "universal $k^{-5/3}$ " shape characterizing the inertial spectrum of freely evolving 3D turbulence. This property has been assessed in numerous experiments of 3D turbulence including wind tunnel experiments and others (Frisch 1995).

Identifying a fluid system as being turbulent generally requires resolving its inertial spectrum. Reproducing this $k^{-5/3}$ shape is now considered a standard benchmark for validating most direct numerical simulations (DNS) which purport to model turbulence. For numerical experiments, in turn, this means capturing *at least* 1–2 decades of the inertial spectrum, i.e., there ought to be a factor of 10–100 scale difference between the injection and dissipation scales. We shall return to this matter and how it bears upon simulations relating to protoplanetary disk turbulence in Sect. 6.

3.3. 2D turbulence

Freely decaying 3D turbulence can be considered a possible end-member state contained in the idealized abstract space of turbulent flows. By its construction, there are no body forces acting upon the fluid. Body forces, like gravity, often act upon the fluid by constraining one dimension or enforcing a symmetry on the flow. One might expect the presence of a body force adds more complexity to the problem and that, in comparison to freely evolving 3D turbulence, even less might be said about the statistical quality of any emergent state. In the idealized case of 2D turbulence, the opposite is true. 2D turbulence is the case of the Navier-Stokes equations in which one dimension is restricted *by fiat* – henceforth we assume it is the z -direction. Atmospheric flow (constrained by both gravity and rotation) and the motion along bubble surfaces (constrained by surface tension) are close, but not exact, physical instances of idealized 2D turbulence.

Such flows are known to support a *double cascade*. The Kraichnan-Batchelor theory of steady driven 2D turbulence says that flows with power injected on some scale ℓ_0 , which is much less than scale of the system L and

much larger than the dissipative scales ℓ_{diss} , will exhibit a *direct cascade of enstrophy* and an *inverse cascade of energy*. With the vorticity as defined ϖ , strictly 2D flow results in

$$\varpi = \varpi_z \hat{z} \equiv \left[\frac{\partial u_x}{\partial y} - \frac{\partial u_y}{\partial x} \right] \hat{z}. \quad (40)$$

Enstrophy is defined to be the square of the vorticity, i.e., $\mathcal{Z} \equiv \varpi^2$. In the inverse cascade regime ($L \geq \ell \geq \ell_0$) the energy spectra has the familiar form, $\mathcal{E} \sim k^{-5/3}$. Unlike the 3D case discussed above, energy shifts from smaller scales to larger scales. Often times this can be identified by eye as the numerical experiment of an unstable 2D shear layer in Fig. 2 shows: a thin vortex strip rolls up under its own induced flow and eventually turns into a larger tumbling structure containing a jumble of fine scale vortex filaments even smaller than the original filament. These developed finer scale filamentary structures qualitatively exhibits the forward cascade of enstrophy. The emergent large scale vortex structure exhibits the inverse cascade of energy.

In the forward enstrophy cascade regime of steady driven 2D turbulence, the wavenumber dependence of the energy spectrum is much steeper, in fact $\mathcal{E} \sim k^{-3}$. These properties are summarized in Fig. 3. The trends predicted in the Kraichnan-Batchelor theory of steady driven turbulence have yet to be disproven (Boffetta & Ecke 2012): the features of the theory summarized in Fig. 3 are asymptotically approached as recent highly resolved DNS indicate (Boffetta & Musacchio 2010).

The direct enstrophy cascade can be rationalized by the following argument. For 2D incompressible Navier-Stokes flow, the equation governing its evolution is greatly simplified to

$$\frac{d\varpi_z}{dt} = \nu \nabla^2 \varpi_z, \quad (41)$$

in which the incompressibility constraint means that all quantities may be expressed in terms of a single scalar, called the streamfunction Ψ , in which

$$u_x = -\frac{\partial \Psi}{\partial y}, \quad u_y = \frac{\partial \Psi}{\partial x}, \rightarrow \varpi_z = \nabla^2 \Psi.$$

If the dissipation scale is indeed very small, then Eq. (41) states that in the inertial range viscosity is negligible and that, consequently, the vorticity is a materially conserved quantity. In this case we can follow the same physically motivated logic administered in our discussion of freely evolving 3D turbulence. By assuming isotropy, homogeneity and self-similarity we state that patches of vorticity can undergo a Richardson type of cascade by preserving the vorticity with which it was endowed. Calling this vorticity ϖ_0 , we find therefore that mother-daughter structures must preserve this quantity all the way down to the dissipation scales, therefore

$$\varpi_0 \sim \frac{u_\ell}{\ell} = \text{constant}, \rightarrow u_\ell = \varpi_0 \ell \sim \varpi_0 k^{-1}. \quad (42)$$

This means that the energy of the structure is $E_k \sim \varpi_0^2 k^{-2}$, which means that in the forward enstrophy cascade zone $\mathcal{E}(k) \sim E_k/k \sim \varpi_0^2 k^{-3}$.

3.4. The quality of turbulence in strongly rotating and stratified flows and Rhines scales

Turbulence in strongly rotating and stratified flows is an unsettled topic. A case in point is the Earth's atmosphere which one might consider to be a close approximation to 2D flow. Nastrom & Gage (1985) analyzed wind data based measurements made on thousands of commercial airplane flights, and they found that the atmosphere indeed exhibits a k^{-3} spectrum on scales ranging from the planetary ($\sim 10,000\text{km}$) through the synoptic scales ($\sim 1000\text{km}$). However, in the mesoscales range, which starts at about 500km and goes down to about a few km, the spectral shape $\sim k^{-5/3}$. While the large scale energy injection mechanism is known (baroclinic instability $\sim 1000\text{ km}$ scales), a robust physical explanation for the $k^{-5/3}$ spectrum, including what are the energy sources and sinks, remains a subject of much debate with several candidate mechanisms, like gravity wave breaking, moist convection and others (Tulloch & Smith 2006; Marino et al. 2014; Sun et al. 2017). While the large scale trend may be rationalized in terms of the inverse cascade picture of driven 2D turbulence, the switch over into what ostensibly exhibits 3D statistical character occurs on length scales that are much larger than the vertical scales of the atmosphere ($\sim 10\text{km}$, corresponding to the height of the tropopause). Similar trends have recently been identified for Jupiter's weather layer based on analysis of imaging data acquired during the Cassini spacecraft's Jupiter gravity assist maneuver (Young & Read 2017).

The inverse cascade is also arrested on the large *Rhines scales*. Rhines (1979) demonstrated that for 2D turbulence on a rotating sphere there exists a scale λ_b spanning the north-south direction on which the differences of the planetary vorticity across this length scale equals the overturn time of the upscale cascading turbulent eddies denoted by $\varpi_{\text{eddy}} \sim \mathcal{U}_b/\lambda_b$. Disturbances in the planetary PV give rise to Rossby waves (as described in Sect. 2.3). If the frequency response of the planetary scale Rossby wave equals that of the turbulent eddy overturn time, then instead of these eddies sending their kinetic energy to larger length scales as demanded by the inverse cascade process, these λ_b -scale turbulent eddies will transfer their energy into large scale Rossby waves⁷. If we assume the turbulent eddies are of longitudinally-latitudinally equi-dimensional, then by setting $k_x = k_y = k_b \equiv 2\pi/\lambda_b$ in Eq. (33), we find that setting $\omega_{\text{RW}} = \varpi_0$ implies

$$\frac{\beta_{\text{PV}}}{2k_b} = \mathcal{U}_b k_b, \quad \rightarrow \quad k_b = \sqrt{\beta_{\text{PV}}/2\mathcal{U}_b}. \quad (43)$$

These special scales are observed in simulations and in data of planetary atmospheres. These large scale waves may themselves nonlinearly develop and/or play a role in generating large scale circulation in the form of global

⁷ Note that a steady rotating global atmosphere sitting atop flat topography will have variations in its potential vorticity as a function of latitude. Potential vorticity will also show variations if there is some amount of significant topography. Thus, large scale inverse-cascading turbulent eddies encountering topography will also result in some of their energy being transferred into Rossby waves. This latter feature is relevant to planetary atmospheres.

zonal flows through the process of wave-mean flow interactions. For a deeper and expanded discussion regarding wave-mean flow processes see Pedlosky (1982) and Vallis (2006). The consequences are clear: systems that are nearly 2D and turbulent, that exhibit both an inverse cascade and other features like strong rotation, can result in the organization of such disorder into global scale organized motions like jets and waves. If protoplanetary disk dynamics indeed exhibits the qualities of 2D turbulence, then there will arise a similarly motivated Rhines scale (Sheehan et al. 1999). We reflect on this further below.

3.5. The alpha disk model

Despite the great abundance of observations and data available for the Earth's atmosphere, an understanding of the nature of its turbulence is still cloudy. The situation with regards to accretion disk turbulence remains much worse – although the developments of the last five years raise hope that inroads toward its characterization is on the near term horizon.

In lieu of this, and for a great many number of years, the astrophysical community has relied on a mixing-length model to represent accretion disk turbulence. The so-called α -disk model (Shakura & Sunyaev 1973; Lynden-Bell & Pringle 1974) takes a heuristic approach toward handling this situation. It assumes that there exists a dynamically sustained process that generates disordered velocity fluctuations about the mean Keplerian state. If these disordered fluctuations are indeed turbulent then they will be engaged in some kind of nonlinear energy transfer which translates into them exhibiting non-zero spatial correlations. These correlations are assessed by calculating spatial averages of the corresponding Reynolds stresses. Following the original example, we consider u'_r and u'_ϕ respectively as the fluctuating radial and azimuthal velocities about the basic Keplerian (azimuthal) velocity $U_K \sim R^{-1/2}$. Denoting spatial averages with overbars, the negative of the averaged radial-azimuthal component of the Reynolds stress is equated with an effective linear momentum diffusion through the following identification:

$$v_t \frac{\partial U_K}{\partial R} \equiv -\overline{u'_r u'_\phi}. \quad (44)$$

The left hand side expression of the above is motivated from the definition of viscosity from the molecular dynamics point of view which says that neighboring parcels of gas will exchange momentum in proportion to the gradient of their localized bulk (mean) velocities. In this case the mean/bulk velocity is taken as the Keplerian one. But the key ingredient in this characterization is the measured correlation $\overline{u'_r u'_\phi}$. Thus, the effective turbulent diffusion (v_t , in units of cm^2/s) is expressed in terms of the product of the local sound speed and scale height: $v_t \equiv \alpha c_s H$. Thus α is the measure of the turbulent intensity and we have

$$\alpha \sim \frac{\overline{u'_r u'_\phi}}{c_s^2}, \quad (45)$$

which follows from the definition of H in Eq. (20). In this

form, α measures the square of the local Mach number of the fluctuating disk velocities which are (presumably) dominated by the velocities of the injection scales.

Quoting this value of α is the main characterization used to assess the *degree of turbulence* in protoplanetary disks. It says nothing about the statistics of the actual small scale motions driven downscale by the larger scale driven dynamics – i.e., to date $\mathcal{E}(k)$ is still not known. This has direct consequences for the accumulation of disk dust.

Nonetheless one may make estimates. Assuming the turbulence is steady and the energy cascade is 3D, as in the sense of Kolmogorov-Obukhov theory, then a cascade rate ε_α based on the measured value of α may be estimated by following the physical reasoning in Sect. 3.2 to be approximately,

$$\varepsilon \approx \varepsilon_\alpha \equiv \delta v^3 / H_{\text{oturn}} = \alpha^{3/2} c_s^3 / H. \quad (46)$$

where we have identified the square of the fluctuation velocities with the Reynolds stress: $\delta u^2 \equiv \overline{u'_r u'_\phi}$.

Implicit in this assumption is that the overturn scales H_{oturn} are approximately that of a scale height. The three large-scale eddy producing linear instabilities described in the upcoming sections generate structures whose fundamental length scales are generally a fixed fraction of the local H . Interestingly, as noted in Sect. 2.1, if the mean temperature profile in a protoplanetary disk Ohmic zone has a value of $q_T < 3/2$, then the scale height H increases with distance and, therefore, the overturn scales similarly enlarge with radial distance from the central star, much inline with von Weizsäcker's predictions (Gamow & Hynke 1945).

If, on the other hand, the protoplanetary disk turbulence exhibits a 2D energy cascade at the largest scales, then energy will cascade until it encounters its corresponding Rhines scale. 3D simulations of buoyant convection in disks performed by Cabot (1996) indeed show that the small scale forcing sends power from the small scales and drives into place 2D large-scale zonal jets. The length scale of the emergent jets from these simulations L_{jet} were shown by Sheehan et al. (1999) to be consistent with the corresponding Rhines scale appropriate to the local disk section. Specifically, characterizing the turbulent large scale eddies by the previously motivated α prescription, then the Rhines scale vortices will have circulation speeds of $\mathcal{U}_b \sim \alpha^{1/2} c_s$. Thus, taking this together with the definition of the Rhines scale found in Eq. (43) and the disk appropriate value of the β_{PV} -parameter found in Eq. (35), then we find that the corresponding predicted value of k_b to be

$$\lambda_b \sim \frac{\pi}{k_b} = \pi \sqrt{\frac{8\alpha^{1/2}}{3}} HR = \pi \sqrt{\frac{8\alpha^{1/2}}{3h}} H. \quad (47)$$

The convective turbulence simulated in Cabot (1996) predicted values of α in the range 10^{-2} to 10^{-4} . Assuming disk aspect ratios $h \sim 0.05 - 0.1$, plugging in these values into Eq. (47) show that λ_b is predicted to be an order one fraction of the local pressure scale height H , which is in rough agreement with the measured values of the jet widths L_{jet} observed to emerge, presumably as the end-state of the inverse cascade of Cabot (1996).

Finally we can estimate the energy cascade rate toward the Rhines scale following the same line of reasoning leading to Eq. (46)

$$\varepsilon \approx \varepsilon_\alpha = \frac{\alpha^{5/4}}{\pi} \sqrt{\frac{3h}{8}} \frac{c_s^3}{H}. \quad (48)$$

4. THE PRIME MOVER: LINEAR INSTABILITY

In this section we review the Rayleigh criterion (Sect. 4.1), the magneto-rotational instability (Sect. 4.3.1), and introduce the hydrodynamical instabilities (Sect. 4.4).

4.1. Rayleigh criterion

The Rayleigh criterion is paramount to understanding what instabilities can be present in the Ohmic zone. Starting from the momentum equations, Eq. (11) and Eq. (12), without the pressure gradient, and restricting ourselves to the midplane

$$\frac{\partial u_R}{\partial t} + u_R \frac{\partial u_R}{\partial R} + u_\phi \frac{\partial u_R}{\partial \phi} - \frac{u_\phi^2}{R} = \Omega^2 R \quad (49)$$

$$\frac{\partial u_\phi}{\partial t} + u_R \frac{\partial u_\phi}{\partial R} + u_\phi \frac{\partial u_\phi}{\partial \phi} + \frac{u_\phi u_R}{R} = 0. \quad (50)$$

We can decompose the flow into base (time-independent) and perturbation in

$$\mathbf{u}(x, t) = \bar{\mathbf{u}}(x) + \mathbf{u}'(x, t), \quad (51)$$

with the base flow $\bar{u}_R = 0$ and $\bar{u}_\phi = \Omega R \gg u'_\phi$, the perturbation equations become

$$\frac{\partial u'_R}{\partial t} - 2\Omega u'_\phi = 0 \quad (52)$$

$$\frac{\partial u'_\phi}{\partial t} + (2-q)\Omega u_R = 0 \quad (53)$$

where

$$q \equiv -\frac{\partial \ln \Omega}{\partial \ln R} \quad (54)$$

Now consider the perturbation as a Fourier mode $\psi' = \hat{\psi}_0 e^{-i(\omega t - k \cdot x)}$, so that

$$-i\omega \hat{u}_R - 2\Omega \hat{u}_\phi = 0 \quad (55)$$

$$-i\omega \hat{u}_\phi + (2-q)\Omega \hat{u}_R = 0 \quad (56)$$

which leads to the solution for the complex eigenfrequency

$$\omega^2 = 2\Omega^2(2-q) \quad (57)$$

This frequency is called epicyclic frequency,

$$\kappa_{\text{ep}} \equiv \Omega \sqrt{2(2-q)} \quad (58)$$

if $q < 2$ then the flow is stable. Since the Keplerian flow has $q = 1.5$, then undisturbed Keplerian flow is unconditionally stable. Attempts at turning the Keplerian flow

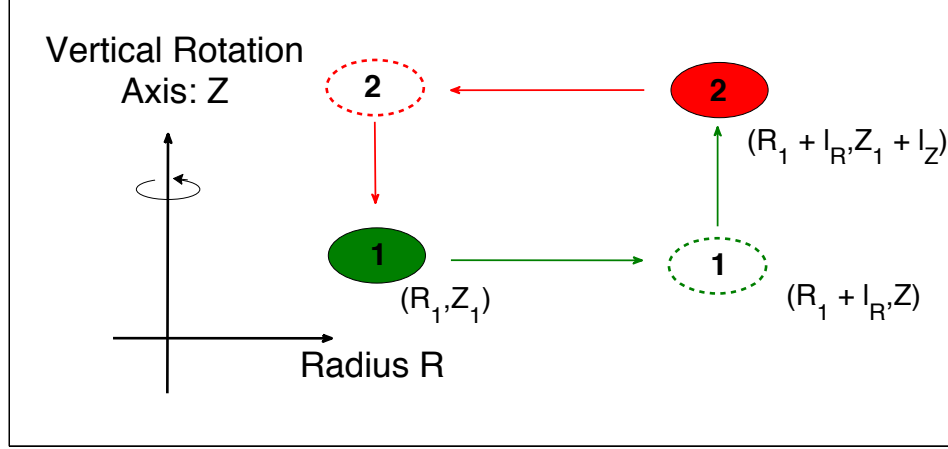


FIG. 4.— Rayleigh instability. Consider two annuli 1 and 2, with the first at radial-vertical position R_1, Z_1 and the second at R_2, Z_2 . The energy argument, as originally found in Kippenhahn et al. (2012) and discussed recently in Lin & Youdin (2015), goes as follows: one interchanges the positions of the two circular annuli by preserving their individual angular momentum. If the total energy of the new system is less upon interchange then setup is regarded as unstable. In the diagram, the fluid ring 1 moves to radial position $R_1 + \lambda_R = R_2$ and then onto vertical position $Z_1 + \lambda_z = Z_2$ while ring 2 executes the opposite motion. A circular final state requires energy dissipation either in the form of heat or radiative losses – a feature that is implicit in this energy argument. In the case of purely barotropic Keplerian flow, which is stable according to this analysis, the interchange in the vertical direction is superfluous as the rotational speeds are the same. The vertical interchange matters when analyzing the conditions for the VSI as the vertical shear in the Keplerian flow figures prominently in driving the instability. Figure adapted from Umurhan et al. (2013).

unstable have to focus on how the Rayleigh criterion is violated.

It is an equivalent statement to the Rayleigh criterion formulated above that angular momentum must increase outward. Given the angular momentum $L = R^2\Omega$, then its derivative is

$$\frac{dL}{dr} = \Omega R(2 - q) \quad (59)$$

and thus the condition $q < 2$ is equivalent to $dL/dR > 0$, i.e., angular momentum should increase with distance. The classical way to understand this criterion is by appealing to an annular ring interchange argument as summarized in the cartoon Fig. 4. Consider two annuli one at an inner radius and disk height, R_1, Z_1 respectively, and the second at an outer radial and disk height position, $R_2 = R_1 + \lambda_R, Z_2 = Z_1 + \lambda_z$ respectively. We posit the following dynamical action: we interchange the positions of the two annuli under the condition that their angular momenta are conserved. We place the interchanged annuli into circular orbits and we assess the new total energy of the configuration. If the energy in this final state is lower than the original arrangement then this new configuration is preferable and the system is unstable. If upon interchange the total energy is higher, then this system is not preferred and the system is stable. The key feature here is that we posit that the annuli are placed into circular orbits and this implicitly means that energy must be either gained or lost by the system as a whole. For barotropic Keplerian flows, the vertical interchange has no effect as the angular momentum is constant on cylinders (i.e., $dL/dZ = 0$) and, thus, the criterion for a lower energy state is equivalent to $dL/dR > 0$. The details of this relatively straightforward analysis may be found in Tassoul (1978) or Kippenhahn et al. (2012).

4.2. The Solberg-Høiland criteria

In the presence of buoyancy, the Rayleigh criterion is substituted for the Solberg-Høiland criteria. These criteria have been derived elsewhere (Tassoul 1978; Abramowicz et al. 1984; Ogilvie 2016), but we repeat it here for completeness largely in part because these criteria figure prominently in the processes discussed in this review. If we include the adiabatic energy equation, stated in terms of pressure,

$$\frac{\partial \rho}{\partial t} + (\mathbf{u} \cdot \nabla) \rho = -\rho \nabla \cdot \mathbf{u}, \quad (60)$$

$$\frac{\partial \mathbf{u}}{\partial t} + (\mathbf{u} \cdot \nabla) \mathbf{u} = -\frac{1}{\rho} \nabla p + \mathbf{g}, \quad (61)$$

$$\frac{\partial p}{\partial t} + (\mathbf{u} \cdot \nabla) p = -\gamma p \nabla \cdot \mathbf{u}, \quad (62)$$

and linearize the system $u_R = u'_R$, $u_\phi = \Omega(R, z)R + u'_\phi$, $u_z = u'_z$, $p = p_0(R, z) + p'$, and $\rho = \rho_0(R, z) + \rho'$, then

$$-i\omega \rho' + u'_R(\partial_R \rho_0 + ik_R \rho_0) + u'_z(\partial_z \rho_0 + ik_z \rho_0) = 0, \quad (63)$$

$$-i\omega u'_R - 2\Omega u'_\phi + \frac{ik_R}{\rho_0} p' - \frac{\rho'}{\rho_0^2} \partial_R p_0 = 0, \quad (64)$$

$$-i\omega u'_\phi + \Omega(2 - q)u'_R + \partial_z(\Omega r)u'_z = 0, \quad (65)$$

$$-i\omega u'_z + \frac{ik_z}{\rho_0} p' - \frac{\rho'}{\rho_0^2} \partial_z p_0 = 0, \quad (66)$$

$$-i\omega p' + u'_R(\partial_R p_0 + \rho_0 c_s^2 ik_R) + u'_z(\partial_z p_0 + \rho_0 c_s^2 ik_z) = 0, \quad (67)$$

where we have also substituted $p_0 = \rho_0 c_s^2 / \gamma$. We define

$$\mathcal{A}_k \equiv c_s \partial_k \ln \rho, \quad (68)$$

$$\mathcal{G}_k \equiv \gamma^{-1} c_s \partial_k \ln p, \quad (69)$$

$$\mathcal{S}_k \equiv \mathcal{G}_k - \mathcal{A}_k, \quad (70)$$

as normalizations of the density, pressure, and entropy gradients in units of frequency. Solving the system yields the dispersion relation

$$\begin{aligned} & \omega^4 - \omega^2 \left[2(2-q)\Omega^2 + \mathcal{A}_z \mathcal{G}_z + \mathcal{A}_R \mathcal{G}_R + c_s^2 (k_z^2 + k_R^2) \right] \\ & + c_s^2 \{ 2(2-q)\Omega^2 k_z^2 - \mathcal{G}_R \mathcal{S}_R k_z^2 - \mathcal{G}_z \mathcal{S}_z k_R^2 \\ & - k_R k_z [2\Omega \partial_z(\Omega r) - \mathcal{G}_z \mathcal{S}_R - \mathcal{G}_R \mathcal{S}_z] \} \\ & + C_1 + iC_2 = 0, \end{aligned} \quad (71)$$

with

$$C_1 = 2(2-q)\mathcal{A}_z \mathcal{G}_z \Omega^2 - 2\mathcal{A}_R \mathcal{G}_z \Omega \partial_z(\Omega r), \quad (72)$$

$$C_2 = c_s (k_z \mathcal{G}_R - k_R \mathcal{G}_z) [2\Omega \partial_z(\Omega r) + \mathcal{A}_z \mathcal{G}_R - \mathcal{A}_R \mathcal{G}_z] \quad (73)$$

Keeping only the leading order terms in c_s , i.e., the c_s^2 terms, we filter out the acoustic modes. The resulting anelastic dispersion relation is

$$\begin{aligned} \omega^2 (k_R^2 + k_z^2) &= k_z^2 \left(\frac{1}{r^3} \frac{\partial L^2}{\partial r} - \mathcal{G}_R \mathcal{S}_R \right) - k_R^2 \mathcal{G}_z \mathcal{S}_z \\ &+ k_R k_z \left(-\frac{1}{r^3} \frac{\partial L^2}{\partial z} + \mathcal{G}_R \mathcal{S}_z + \mathcal{G}_z \mathcal{S}_R \right), \end{aligned} \quad (74)$$

where we substituted $L = \Omega r^2$ for the angular momentum and recognize

$$\kappa_{\text{eq}}^2 \equiv 2(2-q)\Omega^2 = \frac{1}{r^3} \frac{\partial L^2}{\partial r}, \quad (75)$$

$$\kappa_z^2 \equiv 2\Omega \partial_z(\Omega r) = \frac{1}{r^3} \frac{\partial L^2}{\partial z}, \quad (76)$$

as the squares of the epicyclic frequency κ_{eq} and a vertical oscillation frequency κ_z . Notice that we can cast the dispersion relation Eq. (74) into the following matrix form,

$$\omega^2 = \frac{\mathbf{k}^T \mathbf{P} \mathbf{k}}{\mathbf{k}^T \mathbf{k}}, \quad (77)$$

where \mathbf{k} is the disturbance wavevector, and the matrix \mathbf{P} is a 2×2 matrix

$$\mathbf{P} = \begin{bmatrix} A & B \\ C & D \end{bmatrix}, \quad A = -\mathcal{G}_z \mathcal{S}_z, \quad D = \kappa^2 - \mathcal{G}_R \mathcal{S}_R. \quad (78)$$

The partial derivatives of pressure (\mathcal{G}) and entropy (\mathcal{S}) combine into the Brunt-Väisälä frequencies

$$N_R^2 \equiv -\mathcal{G}_R \mathcal{S}_R = -\frac{1}{\rho c_p} \frac{\partial p}{\partial R} \frac{\partial s}{\partial R}, \quad (79)$$

$$N_z^2 \equiv -\mathcal{G}_z \mathcal{S}_z = -\frac{1}{\rho c_p} \frac{\partial p}{\partial z} \frac{\partial s}{\partial z}, \quad (80)$$

so $A = N_z^2$ and $D = \kappa^2 + N_R^2$. As for B and C , there is freedom to choose them from the $k_R k_z$ terms in Eq. (74)

$$B + C = -r^{-3} \partial_z L^2 + \mathcal{G}_R \mathcal{S}_z + \mathcal{G}_z \mathcal{S}_R. \quad (81)$$

Notice that we can construct \mathbf{P} as symmetric by setting $B = C = (B + C)/2$. The eigenvectors of symmetric \mathbf{P} form an orthogonal basis, and \mathbf{k} can be represented from linear combinations of the eigenvectors. Eq. (77) thus means that ω^2 is an eigenvalue of \mathbf{P} . The characteristic equation $\text{Det}(\mathbf{P} - \omega^2 \mathbf{I}) = 0$ is

$$\omega^4 - (A + D)\omega^2 + (AD - B^2) = 0 \quad (82)$$

i.e., a biquadratic with $a = 1$, $b = -\text{Tr}(\mathbf{P})$, and $c = \text{Det}(\mathbf{P})$. The eigenvalues are thus

$$2\omega^2 = \text{Tr}(\mathbf{P}) \pm \sqrt{\text{Tr}^2(\mathbf{P}) - 4\text{Det}(\mathbf{P})} \quad (83)$$

they will be positive if (i) $\text{Tr}(\mathbf{P}) > 0$; and if the square root is always greater than $\text{Tr}(\mathbf{P})$, that is, if (ii) $\text{Det}(\mathbf{P}) > 0$. Conditions (i) and (ii) are the necessary and sufficient conditions for stability. The trace condition gives the first Solberg-Høiland criterion

$$\kappa_{\text{eq}}^2 - \frac{1}{\rho c_p} \nabla p \cdot \nabla s > 0 \quad (84)$$

For the determinant condition, we need to define the term $B = C$. We split the $k_z k_R$ terms in Eq. (74) as

$$B = -\kappa_z^2 + \mathcal{G}_R \mathcal{S}_z, \quad (85)$$

$$C = \mathcal{G}_z \mathcal{S}_R. \quad (86)$$

That $B = C$ follows from the thermal wind equation which can be proven by the following: in equilibrium we have

$$\Omega^2 r \hat{r} = \frac{1}{\rho} \nabla p + \nabla \Phi, \quad (87)$$

and taking the curl of Eq. (87) produces

$$\nabla \left(\Omega^2 r \right) \times \hat{r} = -\frac{1}{\rho^2} \nabla \rho \times \nabla p. \quad (88)$$

The term in the RHS is the baroclinic term. From the definition of entropy we write ρ in terms of p and s

$$\nabla \ln \rho = \frac{1}{\gamma} \nabla \ln p + \frac{1}{c_p} \nabla s, \quad (89)$$

so the baroclinic term is

$$\begin{aligned} \frac{1}{\rho^2} \nabla \rho \times \nabla p &= \frac{1}{\rho c_p} \nabla s \times \nabla p \\ &= \mathcal{S} \times \mathcal{G}. \end{aligned} \quad (90)$$

Substituting Eq. (90) into Eq. (88), we recover for the $\hat{\phi}$ direction

$$-\kappa_z^2 + \mathcal{G}_R \mathcal{S}_z = \mathcal{G}_z \mathcal{S}_R, \quad (91)$$

proving that the matrix \mathbf{P} is symmetric. The determinant condition $\text{Det}(\mathbf{P}) > 0$ becomes

$$-\mathcal{G}_z \mathcal{S}_z (\kappa_{\text{eq}}^2 - \mathcal{G}_R \mathcal{S}_R) + \mathcal{G}_z \mathcal{S}_R (\kappa_z^2 - \mathcal{G}_R \mathcal{S}_z) > 0. \quad (92)$$

Factoring out \mathcal{G}_z from both terms and simplifying reveals

$$-\mathcal{S}_z (\mathcal{S}_z \kappa_{\text{eq}}^2 - \mathcal{S}_R \kappa_z^2) > 0. \quad (93)$$

Substituting for the gradients leads us to the second condition

$$-\frac{\partial p}{\partial z} \left(\frac{\partial s}{\partial z} \frac{\partial L^2}{\partial r} - \frac{\partial s}{\partial r} \frac{\partial L^2}{\partial z} \right) > 0. \quad (94)$$

Eq. (84) and Eq. (94) are the Solberg-Høiland criteria for stability. If either criterion is violated, then it means that there are sets of disturbances – characterized by some range wavevectors k – for which the system must be linearly unstable.

We call attention to an often overlooked consequence of the Solberg-Høiland criteria. The determinant condition $AD - B^2 > 0$ implies that A and D must have the same sign. Since the trace condition $A + D > 0$, then A and D must each be positive, which implies

$$N_z^2 > 0, \quad (95)$$

$$\kappa_{\text{eq}}^2 + N_R^2 > 0, \quad (96)$$

have to be satisfied *independently* for stability. In Eq. (84) the dot product notation is a mathematically compact way to write the condition; physically, the $\kappa_{\text{ep}}^2 + N_R^2$ and N_z^2 terms are working on different modes. If either of them are negative, then the trace can still be positive but the second condition (Eq. 94) is negated.

Eq. (95) is the usual Schwarzschild criterion assessing the buoyant stability of a vertically stratified fluid. Notice that it follows directly from Eq. (74) by setting $k_z = 0$.

Eq. (96), which follows from Eq. (74) by setting $k_R = 0$, states that k_z oscillations that are stable to epicyclic motions can be de-stabilized by buoyancy, and vice-versa. Notice that the criterion is derived for adiabatic motion, so it will be modified in the presence of finite thermal diffusion or cooling, in principle allowing for unstable growth even when the adiabatic criterion is obeyed. Indeed, that is the driving force of the convective overstability (Sect. 4.4.2).

Eq. (94) pertains to the stability of the mixed $k_R k_z$ mode. Violation of Eq. (94) is the driving mechanism for the vertical shear instability, (Sect. 4.4.1).

Physical Interpretation: The Solberg-Høiland criteria may be rationalized in the same way the Rayleigh criterion is understood by appealing to the fluid-ring/parcel interchange analysis motivated in Sect. 4.1. In particular, the contribution to the criterion by the buoyancy term is often referred to as the Schwarzschild criterion: Referring once again to Fig. 4, we consider the angular momentum conserving interchange of the two fluid rings as depicted. In their new interchanged circular orbits, we allow each fluid ring to adiabatically expand

and reach pressure equilibrium with its new environment. As a result of the expansion, the fluid rings now exhibit different densities which are entirely dictated by the entropy gradient of the fluid, as indicated in Eq. (74). This interchanged state is unstable if the total resulting energy – which is now a sum of both the kinetic energy and the gravitational potential energy – is less than what it was in the undisturbed configuration. With respect to Fig. 4, if the gravity vector were pointed down and toward the star (indicated by ∇p), then the interchange would be destabilizing if the adjusted density of parcel 1, having been translated to parcel 2's original position, is less than parcel 2's original density before the interchange. Similarly, the interchange would signal potential instability if the adjusted density of parcel 2, having been translated to parcel 1's original position, is greater than parcel 1's original density before the interchange. Such a resulting density change means that the total gravitational potential energy after the interchange is less than with which it began. We are reminded that the interchange physics ultimately rests on the work done by the system upon the interchanged fluid rings and this work is ultimately measured by the terms $\partial_k p \partial_k s$ found in Eq. (74). Thus, while an adverse entropy gradient is destabilizing according to this energy principle and is the essence of the Schwarzschild criterion, instability of the disk fluid requires that the total energy of the interchanged fluid elements to be less than in the undisturbed state. As such, the Solberg-Høiland criteria, embodied in Eq. (84) and Eq. (94), dictate the properties of the disk gas required to insure that the resulting energy of every possible swapped fluid-ring state is higher than with which it began – hence, predicting a sufficient condition for stability.

4.3. A magnetic interlude

Before introducing the hydrodynamical instabilities, it is instructive to recall the basic physics of the MRI and how it violates the Rayleigh criterion.

4.3.1. Magnetorotational instability

Consider that the gas parcels pertaining to the rings A and B in a Rayleigh-stable situation (upper panel of Fig. 4) are connected by a tether with a restoring force $-Kx$, where K is a spring constant. The equations of motion are

$$\ddot{x} - 2\Omega y + Kx = 0 \quad (97)$$

$$\ddot{y} + (2 - q)\Omega x + Ky = 0 \quad (98)$$

Consider the Lagrangian displacement

$$q(t) = \bar{q} + \zeta(t),$$

with $\bar{q} = 0$ and $\zeta = q_0 e^{i\omega t}$, where q is a generalized coordinate. The derivatives are

$$\dot{q} = i\omega \zeta \quad \text{and} \quad \ddot{q} = -\omega^2 \zeta \quad (99)$$

and the equations of motion are

$$-\zeta_x \omega^2 - 2\Omega \zeta_y i\omega + K\zeta_x = 0, \quad (100)$$

$$-\zeta_y \omega^2 + (2 - q)\Omega \zeta_x i\omega + K\zeta_y = 0. \quad (101)$$

This system is solved to yield the dispersion relation

$$\omega^4 - (2K + \kappa^2)\omega^2 + K(K - 2q\Omega^2) = 0 \quad (102)$$

which is a biquadratic equation. The solution is

$$\omega^2 = \frac{(2K + \kappa^2)^2 \pm \sqrt{4K(K - 2q\Omega^2)}}{2}. \quad (103)$$

If

$$K - 2q\Omega^2 < 0 \quad (104)$$

then ω^2 will have an imaginary component, and thus we have at least one growing root. Eq. (104) is the condition for instability. We see that if $K = 0$ (no tether), the condition for stability is simply $q > 0$, i.e., the angular velocity decreasing outward. This is satisfied in Keplerian disks.

The situation with the tether is identical to how magnetic fields operate. Let us include the Lorentz force in Eq. (2), i.e.,

$$\begin{aligned} \mathbf{F} \rightarrow \mathbf{F}_{\text{Lorentz}} &= \frac{1}{4\pi} (\nabla \times \mathbf{B}) \times \mathbf{B} \\ &= -\nabla \left(\frac{B^2}{8\pi} \right) + \frac{(\mathbf{B} \cdot \nabla) \mathbf{B}}{4\pi} \end{aligned} \quad (105)$$

where \mathbf{B} is the magnetic field. The second line above decomposed the Lorentz force into magnetic pressure and magnetic tension, respectively. Consider now the magnetic tension with a uniform base magnetic field $B_0 \hat{e}$, where \hat{e} is an arbitrary unit vector, upon which we superimpose a Lagrangian field displacement $\mathbf{B}' = B_0 i k \xi$. The resulting acceleration is

$$\frac{B_0 \partial \mathbf{B}'}{4\pi \rho} = -\frac{k^2 B_0^2 \xi}{4\pi \rho} = -(k \cdot \mathbf{v}_A)^2 \xi, \quad (106)$$

where we used $\partial = -ik$ and substituted $\mathbf{v}_A = \mathbf{B} / \sqrt{4\pi \rho}$ for the Alfvén velocity. We see from Eq. (106) that the magnetic tension on the perturbation depends on the negative of the displacement, behaving exactly like a spring, with effective spring constant

$$K \equiv (k \cdot \mathbf{v}_A)^2. \quad (107)$$

Therefore, the instability condition is

$$(k \cdot \mathbf{v}_A)^2 - 2q\Omega^2 < 0 \quad (108)$$

Because the magnetic field appears multiplied by the wavevector, even weak fields generate significant tension at small enough scales. Indeed the MRI is a weak field instability, and should be generally present when the gas is magnetized.

4.3.2. Suppression of the MRI

While full ionization is the state of the hot disks around black holes, protoplanetary disks are cold and poorly ionized, as noted in the introduction. In this case, neutrals compose the bulk of the flow, and ions and electrons drift through them. The magnetic flux is mostly

frozen on the electron fluid, being these the most mobile charge carrier. In the case of a weakly ionized gas, the most probable collision a electron would suffer is with a neutral. These processes enter the induction equation as the electromotive force and Ohmic diffusion, respectively

$$\frac{\partial \mathbf{B}}{\partial t} = \nabla \times (\mathbf{u}_e \times \mathbf{B} - \eta \nabla \times \mathbf{B}), \quad (109)$$

where \mathbf{u}_e is the velocity of the electron fluid and η the Ohmic resistivity. The ratio of the two terms is the magnetic Reynolds number

$$\text{Re}_M = \frac{\mathcal{U} \mathcal{L}}{\eta}, \quad (110)$$

defined on dimensional grounds. Notice the symmetry with the usual (hydro) Reynolds number, with viscosity replaced by resistivity. At any length scale \mathcal{L} , magnetic effects will be suppressed if this quantity falls below unity. The velocity associated with magnetic fields is the Alfvén velocity v_A , and the length of interest is the MRI scale, given by Eq. (108), $k_{\text{MRI}}^{-1} \approx v_A \Omega^{-1}$, so the condition for the operation of the MRI in the presence of resistivity is

$$\Lambda \equiv \text{Re}_M(v_A, k_{\text{MRI}}) = \frac{v_A^2}{\Omega \eta} > 1 \quad (111)$$

where we defined the *Elssasser number*, Λ , the magnetic Reynolds number associated with the MRI.

Of course, Ohmic resistivity, the drag between electrons and neutrals, is not the only impediment to magnetic coupling. As also stated in the introduction, the drift between electrons and ions when ions are coupled to the neutrals (Hall effect) and ions and neutrals when ions are coupled to the electrons (ambipolar diffusion) are the two other non-ideal effects. We can decompose the electron velocity \mathbf{u}_e in terms of the ion and neutral velocities \mathbf{u}_i and \mathbf{u} as (Wardle & Königl 1993; Balbus & Terquem 2001)

$$\mathbf{u}_e = \mathbf{u} + (\mathbf{u}_e - \mathbf{u}_i) + (\mathbf{u}_i - \mathbf{u}) \quad (112)$$

the first term is the reference frame velocity (following the neutrals). The second is the Hall effect and the third is ambipolar diffusion. If we consider a singly ionized species, the current $\mathbf{J} = \sum_j n_j Z_j e \mathbf{u}_j$, where e is the elementary charge and n_j and $Z_j e$ are respectively the number density and charge of species j , becomes

$$\mathbf{J} = n_i e (\mathbf{u}_i - \mathbf{u}_e) \quad (113)$$

As for the ambipolar term, in collision equilibrium the drift between ions and neutrals is set by, in the ion equation of motion, equating the Lorentz force with the neutral-ion collisional drag (Balbus & Terquem 2001; Bai & Stone 2017), so that

$$\frac{\mathbf{J} \times \mathbf{B}}{c} = \gamma_i \rho_i \rho (\mathbf{u}_i - \mathbf{u}) \quad (114)$$

and Eq. (115) can be cast as

$$\mathbf{u}_e = \mathbf{u} - \frac{\mathbf{J}}{n_i e} + \frac{\mathbf{J} \times \mathbf{B}}{c \gamma_i \rho_i \rho'}, \quad (115)$$

where c is the speed of light. The induction equation then becomes

$$\frac{\partial \mathbf{B}}{\partial t} = \nabla \times \left[\mathbf{u} \times \mathbf{B} - \frac{4\pi \eta \mathbf{J}}{c} - \frac{\mathbf{J} \times \mathbf{B}}{n_e e} + \frac{(\mathbf{J} \times \mathbf{B}) \times \mathbf{B}}{c \gamma_i \rho_i \rho'} \right] \quad (116)$$

We can cast the Hall and ambipolar terms in terms of an effective resistivity and a current, similarly to the Ohmic term

$$\frac{\partial \mathbf{B}}{\partial t} = \nabla \times \left\{ \mathbf{u} \times \mathbf{B} - \frac{4\pi}{c} \left[\eta_O \mathbf{J} + \eta_H \frac{\mathbf{J} \times \mathbf{B}}{B} + \eta_A \frac{\mathbf{B} \times (\mathbf{J} \times \mathbf{B})}{B^2} \right] \right\} \quad (117)$$

where we now switched $\eta \rightarrow \eta_O$ for symmetry. Comparing Eq. (116) and Eq. (117), the Hall and ambipolar resistivities are

$$\eta_H = \frac{Bc}{4\pi n_e e} \quad (118)$$

$$\eta_A = \frac{B^2}{4\pi \gamma_i \rho_i \rho'} \quad (119)$$

We quote the Ohmic resistivity for completeness (Krall & Trivelpiece 1973; Balbus & Terquem 2001; Warde 2007; Lesur et al. 2014)

$$\eta_O = \frac{m_e c^2}{4\pi e^2} \frac{n}{n_e} < \sigma_{\text{coll}} u >_e \approx 234 x^{-1} T^{1/2} \text{ cm}^2 \text{ s}^{-1} \quad (120)$$

where m_e is the electron mass, x is the ionization fraction, σ_{coll} is the cross section of electron-neutral collisions, and the angled brackets represent averaging over the Maxwellian velocity distribution of the electrons. The resistivities allow for the definition of Hall and ambipolar Elsasser numbers, in symmetry with the Ohmic Elsasser number.

$$\Lambda_H \equiv \frac{v_A^2}{\Omega \eta_H} = \frac{en_e B}{c \rho \Omega} \quad (121)$$

$$\Lambda_A \equiv \frac{v_A^2}{\Omega \eta_A} = \frac{\gamma_i \rho_i}{\Omega} \quad (122)$$

In general, the MRI will be present if all Elsasser numbers are larger than unity. The dominant resistive effect is that of lowest Elsasser number. For the Minimum Mass Solar Nebula model (MMSN, Hayashi 1981) and uniform ionization fraction we can write

$$\Lambda_O = 3.2 \times 10^{-6} x_{13} \beta_4^{-1} \rho_9^{-1} T_{300}^{-1/2} R_{\text{AU}}^{5/4} \quad (123)$$

$$\Lambda_H = 3.2 \times 10^{-5} x_{13} \beta_4^{-1/2} (\mu/2)^{-1} R_{\text{AU}}^{-1/8} \quad (124)$$

$$\Lambda_A = 1.4 \times 10^{-2} x_{13} \rho_9 R_{\text{AU}}^{-5/4}. \quad (125)$$

where x_{13} means ionization fraction in units of 10^{-13} , β_4 the plasma beta parameter ($\beta \equiv 2cs^2/v_A^2$) in units of 10^4 , ρ_9 the gas volume density in units of 10^{-9} g/cm^3 , T_{300} the temperature in units of 300 K, and R_{AU} the distance in AU. Under the approximations made, at 1AU in the MMSN, Ohmic resistivity will be the dominant impedance, but the problem is very model-dependent, and different combinations will yield different Elsasser numbers at different radii. The resistivities do not consider either the presence of grains, which will modify them (Turner & Drake 2009, but see Simon et al. (2018) for a different opinion).

We assume that the disk will have a region that is Ohmic-dominated, and concentrate from now on our analysis on this region.

4.3.3. An interlude within an interlude: Pure Hall MHD and Generalized Potential Vorticity

Under conditions in which both the Ohmic and Ambipolar coefficients are greatly dominated by the Hall term, i.e. when $\eta_O \ll \eta_H$, and $\eta_A \ll \eta_H$, we might consider the induction equation (Eq. (117)) in the identical limit $\eta_O = \eta_A = 0$ and find that it reduces to

$$\frac{\partial \mathbf{B}}{\partial t} = \nabla \times \left(\mathbf{u} \times \mathbf{B} - \frac{m_e}{xe} \frac{\mathbf{J} \times \mathbf{B}}{\rho} \right), \quad (126)$$

where we have restored the terms defining η_H . If we assume the following, (i) x is a constant, (ii) $\mathcal{Q} = 0$ which means that the gas entropy is materially conserved, and (iii) we neglect gas viscosity by setting $\mathbf{T} = 0$, then Holm (1987) showed that combining Eqs. (1-2) and Eq.(8) with Eq. (126) reveals that the Hall MHD equation set possesses a magnetic generalization of Ertel's theorem. In particular, there exists a magnetic generalization of potential vorticity, denoted by Ω_{GPV} , which is materially conserved by the flow. That is to say the scalar

$$\Omega_{\text{GPV}} \equiv \frac{1}{\rho} \left(\boldsymbol{\omega} + \frac{xe}{4\pi m_e} \mathbf{B} \right) \cdot \nabla s, \quad (127)$$

obeys the conservation equation

$$\left(\frac{\partial}{\partial t} + \mathbf{u} \cdot \nabla \right) \Omega_{\text{GPV}} = 0. \quad (128)$$

In the limit where the ionization fraction goes to zero, Eq. (127) indicates that Ω_{GPV} limits to the classical conservation of fluid vorticity, $\Omega_{\text{PV}} \equiv \rho^{-1} \boldsymbol{\omega} \cdot \nabla s$ as discussed in Sect. 2.3. The magnetic generalization of the potential vorticity quantity has been used to better understand the emergence and stability of flow structures in confined plasmas. Similar explorations of the role this quantity plays in the emergence of zonal flows in accretion disks subject to Hall MHD have yet to be fully explored.

4.4. Hydrodynamical instabilities

Since the ionization level required to couple the gas to the ambient field is not always met (Blaes & Balbus 1994), it leads to zones that are "dead" to the MRI (Gammie 1996; Turner & Drake 2009). So, the quest for hydrodynamical sources of turbulence continues, if only to provide accretion through this dead zone. In this

section, we describe the three hydrodynamical instabilities discovered in the past few years and that may play a role in disk dynamics in the Ohmic zone. In the next subsection we present the Vertical Shear Instability (VSI), followed by the Convective Overstability (COV), concluding with the Zombie Vortex Instability (ZVI).

Key to all of the following instabilities is the question of the thermal cooling times of the primary perturbations that lead to the widespread instability. For disks this is controlled by radiative processes. Radiation driven thermal relaxation will have two natural limits depending upon the photon mean free path. We define κ_R to be an effective *material* Rosseland opacity (cm^2/g), in other words, a frequency integrated absorption cross section that accounts for the cumulative absorption by both gas and dust per gram. Letting ρ be the mass density of the local disk material, then the relaxation times will depend upon how greatly $l_{\text{rad}} \equiv (\kappa_R \rho)^{-1}$ exceeds the length scale of interest, ℓ , which is the length scale of a fluid disturbance. When $l_{\text{rad}} \gg \ell$ then the thermal relaxation is optically thin while when $l_{\text{rad}} \ll \ell$ then the thermal relaxation is optically thick. The thermal relaxation times τ_r are then given by the following approximate form, based on the exact formulation found in Lin & Youdin (2015) based on the derived expression found in Spiegel (1957),

$$\tau_r = \begin{cases} \frac{3\kappa_R \rho^2 c_V \ell^2}{16\sigma_{\text{SB}} T^3}; & l_{\text{rad}} \ll \ell; \\ \frac{c_V}{16\kappa_R \sigma_{\text{SB}} T^3}; & l_{\text{rad}} \gg \ell; \end{cases} \quad (129)$$

where σ_{SB} is the Stefan-Boltzmann constant. Obviously, the ℓ^2 dependence in the optically thick regime reflects the diffusive nature of the optically thick limit.

These two limits are captured in the two extreme thermal relaxation models. The optically thin limit is often referred to as Newton's Law of Cooling in which the source term \mathcal{Q} in Eq. (8) is given by

$$\mathcal{Q} = \frac{1}{\tau_r} (T_d - T), \quad (130)$$

where T_d is some spatially specified forcing temperature representing how the disk gas is forced by the radiation field from the star, where T in τ_r gets replaced with T_d . In the optically thick limit, the heat source/loss term in Eq. (8) is expressed as a radiative diffusion expression commonly known as the Eddington Approximation,

$$\mathcal{Q} = \nabla \left(\frac{a_{\text{rad}} c}{3\kappa_R} \nabla T^4 \right), \quad (131)$$

where $\sigma_{\text{SB}} \equiv a_{\text{rad}} c / 4$, and a_{rad} is the radiation density constant.

4.4.1. Vertical Shear Instability

The vertical shear instability, as the name suggests, draws on the free energy of vertical shear in disks. According to the Taylor-Proudman theorem, rotating barotropic flows under the action of a central conservative force must exhibit constant rotation on cylinders. By barotropic we mean to say that the fluid pressure is

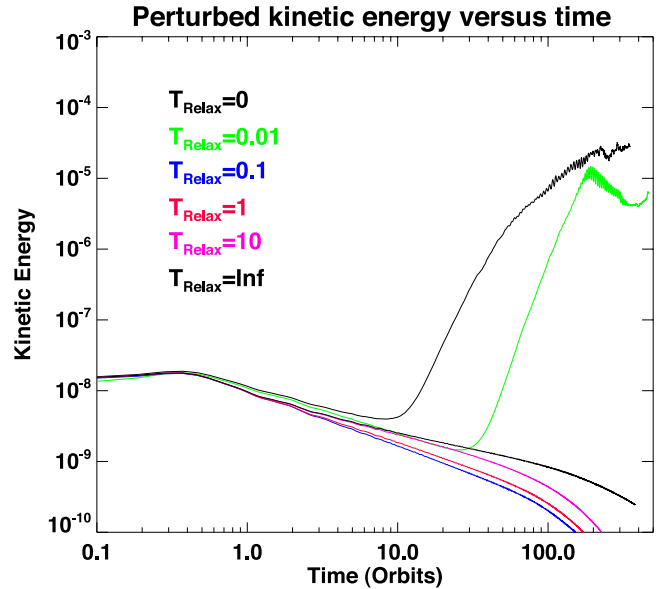


FIG. 5.— Time evolution of the sum of the (normalized) perturbed radial and meridional kinetic energies in disks where the temperature was initially constant on cylinders, as a function of the thermal relaxation time (optically thin cooling law), in units of orbital period, $2\pi\Omega^{-1}$. Note that only the cooling times of 0 and 0.01 cases show growth. Reproduced from Nelson et al. (2013a).

only a function of density, $p = p(\rho)$, as is the case in adiabatic flows in which the fluid temperature may be written as a function of density. Under strong stellar irradiation, like in many parts of protoplanetary disks, the temperature field is mainly a function of the (cylindrical) radius from the central star, exhibiting very little variation in the disk-vertical extent containing most of its inertia. Therefore, because temperature and density isolines do not coincide, the flow configuration is said to be baroclinic which means $\nabla p \times \nabla \rho \neq 0$. Under such baroclinic circumstances, a small amount of vertical shear can be sustained.

As evident in Eq. (28), the shear is proportional to the radial temperature gradient, in a way that the angular speed and momentum is lowest at the midplane and increases in the disk normal directions.⁸

So long as some physical agent maintains this baroclinic configuration (like strong thermal forcing with gravity), then there may exist a condition in which an angular momenta conserving interchange of two annular gas rings of infinitesimal cross-section can result in a lower total energy state (Tassoul 1978; Kippenhahn et al. 2012). This is the physical rationalisation of the Rayleigh stability of barotropic Keplerian flows, e.g., as discussed in Sect. 4.1: as the vertical uniformity of the mean flow state means only evaluating purely radial interchanges. As it happens to be the case for Keplerian flows with $\Omega \sim R^{-3/2}$, this act results in a higher energy configuration and, thus, is not preferable state and the system will want to return to its original configuration.

⁸ This is because the temperature decreases with radial distance. If the radial temperature profiles were to increase, then the situation would be reversed with angular speeds and momenta decreasing with increases away from the mid-plane in the disk normal direction.

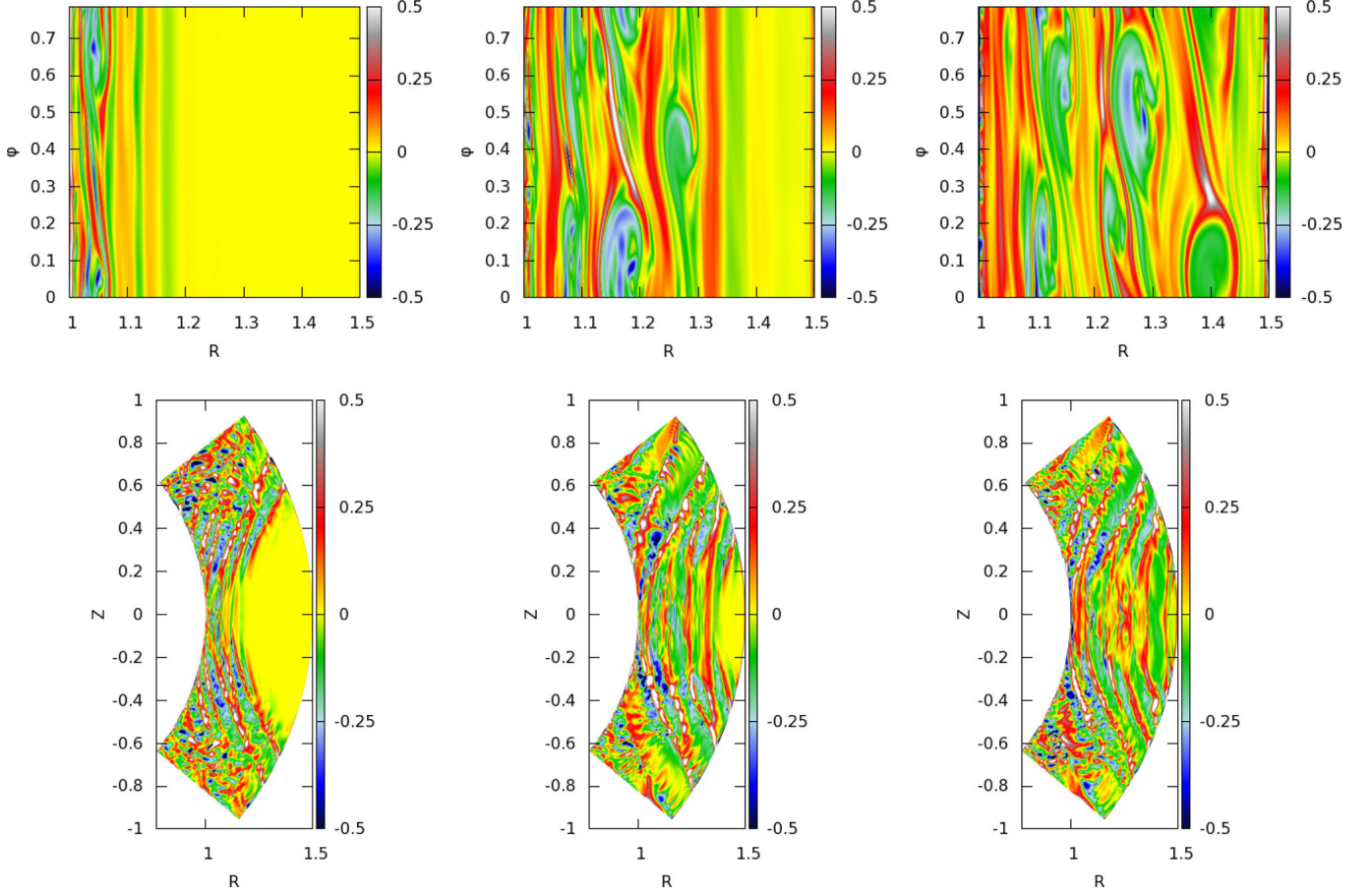


FIG. 6.— Midplane and meridional plane vorticity profiles of the VSI in models utilizing the simple Newton’s Law of Cooling formalism. Snapshots shown: after 201, 317 and 401 orbital periods. In these models $h \equiv H/R = 0.2$ and cooling time $\tau = 0.5\text{orb}$. Figures are reproduced from Richard et al. (2016).

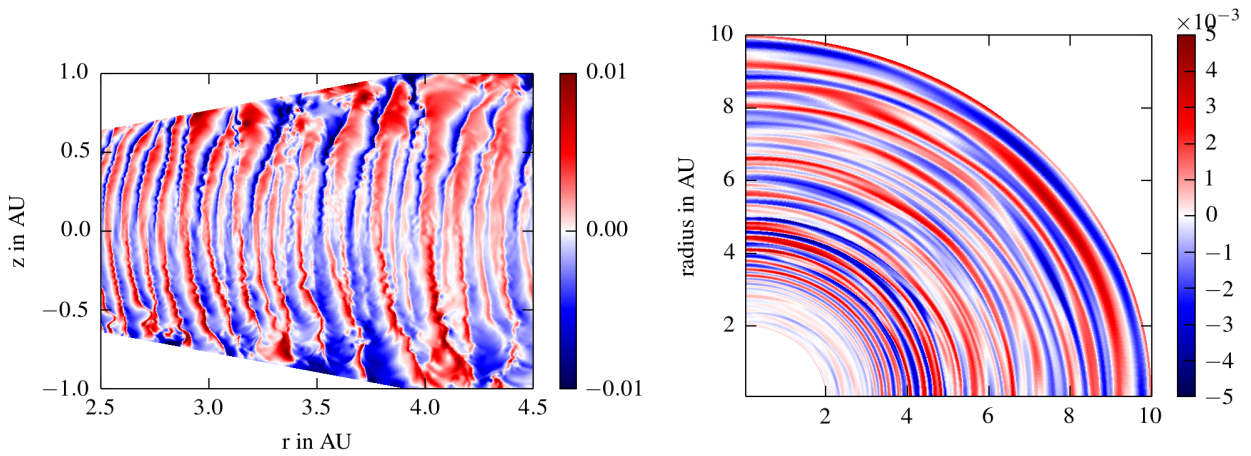


FIG. 7.— Simulations of the VSI with a realistic radiative transfer model (Stoll & Kley 2014). Left: Velocity in the meridional direction, u_θ , in units of local Keplerian velocity for an isothermal simulation without viscosity. The vertical velocities follow a similar pattern. Right: the vertical velocity in the midplane of the disk for a 3D model after 4000 orbits. The nearly axisymmetric property of the saturated instability, even in the ostensibly statistically steady state, is clearly visible in these and in simulations of Nelson et al. (2013b). Figure reproduced from Stoll & Kley (2014).

This is one way toward understanding both the Solberg-Høiland criteria as well as the physics of axisymmetric disk inertial oscillations (which play a further role below).

When thermal and viscous diffusion are an important feature of the physics, then the flow is now baroclinic and the stability properties of rotating flows are no longer controlled by the Solberg-Høiland criteria. Because the mean-flow now exhibits some vertical variation, a physical interchange of the type just described could lead to a configuration with a lower total energy, see once again Fig. 4. *With the restriction of an everywhere isentropic and incompressible gas* subject to wave-like perturbations of the form $\exp(ik_R R + ik_z z)$ in which k_R and k_z are respectively wavenumbers in the radial and disk-vertical directions, a modified stability criterion, obtained originally by Goldreich & Schubert (1967) and Fricke (1968), in application to the radiative zones of differentially rotating stars, says that instability is possible when

$$\frac{\partial L^2}{\partial R} - \frac{k_R}{k_z} \frac{\partial L^2}{\partial z} < 0, \quad (132)$$

where L is the angular momentum. Because for baroclinic disks the rotation rate is a function of both R and z , unstable modes are guaranteed to exist since wavevectors with ratios k_R/k_z that satisfy equation Eq. (132) can always be found. For a thin quasi-Keplerian disk, according to Eq. (132) instability occurs for modes satisfying $k_R/k_z > h^{-1}$, i.e. $\lambda_R < h\lambda_z$, meaning that unstable modes will have radial wavelengths that are much shorter than vertical ones. The instability can be understood through the mathematical lens of the second of the Solberg-Høiland criteria, Eq. (96). Furthermore, the instability can be physically seen as arising directly as a consequence of the ring-parcel interchange diagnostic described in Sect. 4.2. While a purely barotropic Keplerian flow is Rayleigh stable, the interchange procedure can result in a lower energy state after both a radial and a vertical translation of the fluid rings.

Under conditions in which the thermal relaxation times are extremely short ($\tau_r \Omega \ll 1$), the above criterion determines the onset of instability. The possibility that this process is possible for protoplanetary disks was first suggested in the analyses of Urpin & Brandenburg (1998) and Urpin (2003), followed by the study of Arlt & Urpin (2004a) who gave the first estimate of the growth rate to be

$$\sigma \sim |q|h\Omega_0. \quad (133)$$

The first unambiguous identification of the instability in a realistic disk model came in the study of Nelson et al. (2013a)⁹. In this work it was found that oscillating inertial modes become unstable (overstable) and the fastest growing *body modes* have a corresponding radial wavelength $\lambda_R \approx \pi h H_0$. Body modes are inertial modes whose power is concentrated around the midplane of the disk and, therefore, constitutes responses affecting

⁹ Arlt & Urpin (2004b) also performed nonlinear simulations but the disk model they adopted assumed a Boussinesq equation of state. The instability, though technically present, is difficult to identify. Also, using the Boussinesq equation of state predicts that onset to instability occurs at zero frequency, failing to capture the actual oscillatory nature of the VSI at onset.

the bulk inertia of the disk mass. A linear analyses in the infinitely fast relaxation time limit (i.e., $\tau_r \rightarrow 0$) found in Barker & Latter (2015a) confirm the growth rate trends reported earlier while raising concerns about the appearance of surface modes¹⁰, while the analysis in Umurhan et al. (2016a) verified that wavemode with the fastest growth rates should occur for finite values of the radial disturbance wavelength, i.e.,

$$\lambda_R(\max) = \pi|q|hH_0, \quad \sigma(\max) = \sqrt{m}|q|h\Omega_0/4, \quad (134)$$

where m order the sequence of vertical nodes in the responses. All disturbances with odd values of m are called *corrugation modes*, since the disturbance vertical velocities are symmetric about the midplane. Responses with even powers of m are termed the *breathing modes* in which the vertical velocities are symmetric with respect to the midplane. The $m = 1$ and $m = 2$ mode are the respective fundamental responses – these contain the majority of the energy in developing VSI. All normal modes with $m > 2$ (the overtones) increasingly exhibit power concentrated further away from the disk midplane. An immediate consequence is that a majority of the disk motions are projected onto the two fundamentals with very little energy associated with higher overtones. Nonetheless, the linear theory demonstrates that modes show increased growth rates with increasing node number m and this, in turn, raises some concerns. Nonlinear numerical simulations show that only the two fundamental modes get expressed as the process grows. It is possible that the faster growing high vertical node modes, with increased vertical structure with distance from the disk midplane – saturate at low amplitudes are are suppressed by actual and numerical viscosity. For a further discussion on this mathematical matter see Barker & Latter (2015) and Umurhan et al. (2016b).

The nonlinear simulations of the VSI reported in Nelson et al. (2013b) showed several features of the instability as it develops into a nonlinear saturated state. They show that early stages of growth is dominated by the fundamental breathing mode but eventually growth switches over to the fundamental corrugation mode. As such, these two fundamental modes probably constitute the primary injection scales of the resulting turbulence. When the system reaches a quasi-steady state, the radial scales of the resulting structures are much larger than the radial scales of the fastest growing modes, the latter being approximately H or slightly larger, and being highly suggestive of some amount of inverse energy cascade happening on these scales – but this has yet to be quantified. The simulations reported in both Nelson et al. (2013b) and Richard et al. (2016) utilize the simple thermal "Newton's Law of Cooling" model in which the gas is locally forced to a prescribed radial temperature

¹⁰ Nelson et al. (2013b) and Barker & Latter (2015b) identified two classes of modes. In addition body modes, a second class of so-called *surface modes* were also identified. These are structures both attached and concentrated on the vertical boundaries of simulations, and they have fast growth rates. However, owing to the very low densities at these locations they hardly affect the emerging dynamics in the bulk of the disk since they contain very little energy and, as such, are considered artefacts of imposing artificial boundary conditions (Umurhan et al. 2016a).

profile on a cooling time τ_c , usually measured in units of local orbit times ($\text{orb} = 2\pi/\Omega_0$). Nelson et al. (2013b), who run simulations with $h = 0.05$, find that the VSI is most robust for $\tau_c \rightarrow 0$ and will operate with decreasing vigor up to a maximum cooling time $\tau_c = 0.1\text{orb}$. Richard et al. (2016) show that the instability survives for up to larger values of τ_c for correspondingly larger value of h , e.g., see Fig. 7.

When non-isothermal effects are introduced (i.e., $\tau_r > 0$), buoyancy stabilizes otherwise unstable oscillations, according to the Solberg-Høiland criterion. For this reason, it is the exactly-isothermal response ($\tau = 0$) that is most unstable one, and the instability ceases to exist when even moderate levels of adiabaticity are introduced, as shown in Fig. 5. Lin & Youdin (2015) quantify the cooling time requirement for vertically isothermal stratification as

$$\Omega_k \tau_c < \frac{h|q|}{(\gamma-1)} \quad (135)$$

where γ is the ratio of specific heats. The growth rates rapidly diminish and shutoff entirely once cooling times get much longer than this longer cooling times because the unstable wavelength is shifted deep into the viscous range. Furthermore, we observe that this condition is valid for the locally isothermal background state. For vertical adiabatic structures, cooling requirements are less stringent.

Noting that disks are likely optically thick on the length scales on which the VSI operates, Nelson et al. (2013b) equated the critical cooling time ($\tau_c \sim 0.1\text{orb}$) to a corresponding radiative (diffusive) relaxation time predicting that the VSI ought to be operative for effective disk opacities $\kappa < \kappa_c \approx 1\text{cm}^2/\text{gm}$. Subsequent realistic simulations handling the thermal response of the gas using a radiative diffusion model have been performed by Stoll and collaborators (Stoll & Kley 2014, 2016; Stoll et al. 2017a,b). In particular, the important study of Stoll & Kley (2014) demonstrated that the VSI remains robust in such realistic models and, furthermore, they show that its turbulent intensity is of medium strength (see further below), arguing also that it likely plays a significant role in the planet formation process as parts of disks in which dust growth occurs likely support the conditions in which this process operates (see also Flock et al. 2017).

The 3D modeling of the VSI (Nelson et al. 2013b; Stoll & Kley 2014; Richard et al. 2016; Flock et al. 2017) shows that it develops into long-lived unsteady activity. Is it turbulence? At this stage it is not clear. Large scale unsteady vortices are typical of the final emergent structures. Despite the successes of these simulations, an inertial range has yet to be resolved since in most simulations the injection scales are resolved up to 10-20 grid points. The need to flesh out the inertial range of this process forms the basis of future directions on the subject. Nonetheless, the global high-resolution modeling, in particular of Richard et al. (2016); Flock et al. (2017) have quantified the resultant turbulent speeds as being a few percent of the local sound speed – meaning to say that the midplane ($\alpha \approx 4 \times 10^{-5} - 10^{-3}$), increasing to about 20% ($\alpha \approx 10^{-2} - 10^{-1}$) in the corona (i.e., $|z| > 4H_0$). Note that the rise in the apparent values of α far from the

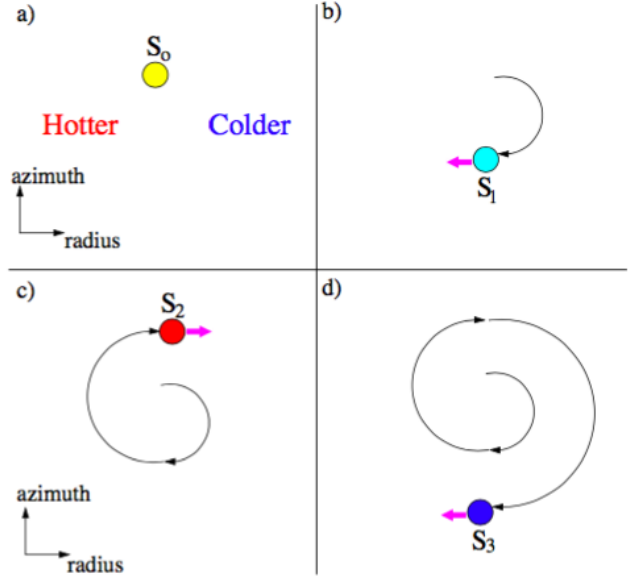


FIG. 8.— A cartoon in four panels indicating the convective overstability mechanism. In panel (a) a fluid blob is embedded in a radial entropy gradient. In panel (b) it undergoes half an epicycle and returns to its original radius with a smaller entropy than when it began $s_1 < s_0$. It hence feels a buoyancy acceleration inwards and the epicycle is amplified. The process occurs in reverse once the epicycle is complete, shown in panel (c), where now $s_2 > s_0$. The oscillations hence grow larger and larger. The impression of two-dimensionality is deceptive. To conserve mass, a similar motion must happen in another horizontal layer, in the opposite direction. This requires $k_z \neq 0$. Reproduced from Latter (2016).

midplane is attributable to the corresponding decrease of the mean densities there.

Lastly, there are apparently two co-acting secondary transition routes into unsteady activity - one attributable to the roll-up of vortices due to vertical motions of the disk and to azimuthal motions in the plane of the disk: Latter & Papaloizou (2018) show in a Boussinesq model that the saturation of the VSI into azimuthally oriented vortices occurs via parasitic Kelvin-Helmholtz modes (Goodman & Xu 1994), while Richard et al. (2016) postulate that a second secondary transition occurs via the Rossby wave instability (Lovelace et al. 1999; Li et al. 2001), leads to continual generation of vertically oriented unsteady vortices. Indeed, Manger & Klahr (2018) have recently found that long lived vortices can be seeded via RWI in a VSI-unstable disk, provided that the azimuthal domain is large enough ($\geq 180^\circ$). And finally, with respect to the secondary transition by the Rossby wave instability, it should be noted that the manner in which the basic zonal flows emerge – upon which this secondary instability operates – has yet to be fully understood but it is possible that an inverse-cascade like the Rhines mechanism might be partly responsible.

4.4.2. Convective Overstability

The second hydrodynamical instability discovered is the convective overstability, which, as the name suggests, is a convective process. It contrasts with classical convection because the direction it occurs is the radial, not the vertical one. It manifests itself as epicyclic oscil-

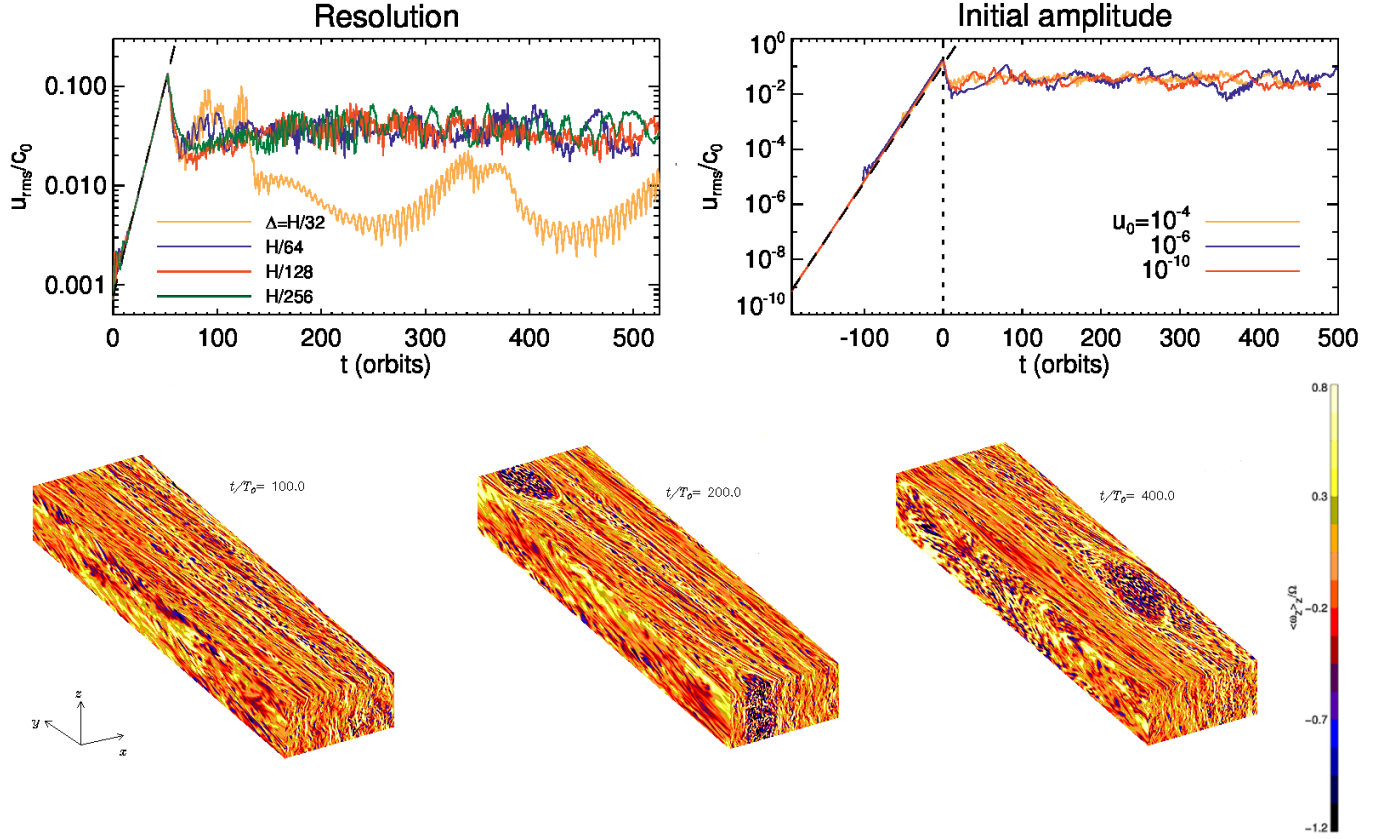


FIG. 9.— Linear and nonlinear evolution of the convective overstability. Upper panels: Convergence study with resolution (left) and initial amplitude of perturbation (right). Resolution of 64 points per scale height is enough to resolve the overstability, and initial amplitudes as small as 10^{-10} times the sound speed (c_0) are enough to lead to growth, demonstrating the linear nature of the process. The linear growth rate (black dashed curve) is well reproduced in all cases. Lower panels: With the linear overstability raising the amplitude of the initial fluctuations to nonlinear levels, a large-scale vortex is generated. The panels show the vertical vorticity. The Reynolds stress saturates at $\alpha \approx 10^{-3}$. Adapted from Lyra (2014).

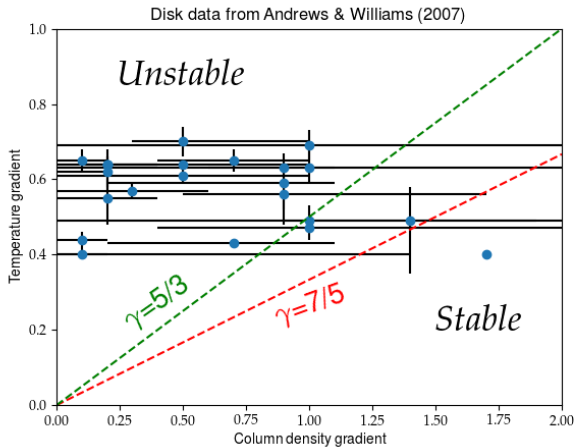


FIG. 10.— The sign of the square of the Brunt-Väisälä frequency defines the stability criterion, here shown as a function of the density and temperature power-law indices. The plot shows the lines for two values of γ . Above (below) the respective line the system is unstable (stable). Adapted from Lyra (2014). The dots represent some disk data for which temperature and density gradients have been estimated. The SBI may be an important process for the majority of disks in the sample.

lations that are amplified by buoyancy, hence the name.

The COV shares many similarities with the subcritical baroclinic instability (SBI), a process discovered earlier, when Klahr & Bodenheimer (2003), modeling disks with negative entropy gradients, found baroclinic growth of vortices. No linear growth was found in linear analysis (Klahr 2004), hinting at nonlinear origin. The nature of the instability was clarified in the works of Petersen et al. (2007a,b), who highlighted the importance of finite thermal inertia. When the thermal time is comparable to the eddy turnover time, the vortex is able to establish an entropy gradient around itself that compensates the large-scale entropy gradient that created it. The mechanism was elucidated by Lesur & Papaloizou (2010): the cycle starts with a fluid parcel buoyantly lifted to an outer orbit. As it travels outwards, it finds itself surrounded by gas of lower entropy. The resulting buoyancy lifts it even further outwards. Deflected by the Coriolis force and following the vortex streamline, the fluid now travels along the azimuthal direction. In this leg, the fluid thermalizes, cooling down. As it cools, it gets denser, and sinks back inwards. The last azimuthal leg will thermalize the fluid, heating it back to the temperature it had in the beginning, closing the cycle. The original radial entropy gradient and the azimuthal temperature gradient established by the thermalization lead

to a non-zero baroclinic term $\nabla p \times \nabla \rho$, generating vorticity locally and amplifying the vortex. A respectable amount of angular momentum is transported by spiral density waves excited by the vortex (Heinemann & Papaloizou 2009, 2012), leading to α values in the vicinity of 10^{-3} .

Notice that the process requires the radial entropy gradient and the radial pressure gradient to be aligned (to give buoyancy) and thermal relaxation or diffusion (to establish the azimuthal gradient). If the gas is locally isothermal a gas parcel has always the same temperature as the surroundings and buoyancy cannot act to amplify the motion. If the gas is adiabatic a gas parcel cannot exchange heat so an outward/inward motion cannot thermalize and return to its equilibrium position. The SBI operates optimally for cooling times similar to the dynamical time.

The convective overstability obeys practically the same mechanism. Indeed, Klahr (2004) had already noted that the SBI could be regarded as a convective instability in the radial direction, but modified by rotation and shear. The difference is the unstable mode. While the SBI uses a large scale vortex, in the COV the fluid executes a small epicycle. This unveils also a crucial difference between the two mechanisms: while the SBI is nonlinear, the COV is linear. The cartoon of Fig. 8 illustrates the growth of a particular mode. As a gas parcel moves into areas colder (hotter) gas, it loses (gains) heat, compresses (expands), and because of the extra buoyancy, overshoots the original amplitude of oscillation. The cartoon is illustrative and does not exactly represent the 3D axisymmetric most unstable mode. Being axisymmetric, the motion is 1D, not necessitating the azimuthal direction. The need for the vertical direction, shown by the k_z dependency in the dispersion relation comes about because of mass conservation: if a gas parcel moves inwards, an equal amount of gas must move outwards. In order to conserve mass, the motion shown in the cartoon must be matched by the same motion executed in another horizontal layer, in the opposite direction.

The overstability exists both if the cooling is provided by thermal relaxation (Lyra 2014) or by thermal diffusion (Latter 2016). In the case that the cooling time τ_r is finite, the Rayleigh and the Solberg-Høiland criteria are but the isothermal and adiabatic limits of the more general anelastic dispersion relation (Klahr & Hubbard 2014; Lyra 2014; Latter 2016)

$$\omega^3 + \frac{i}{\gamma\tau_r}\omega^2 - \omega(\kappa^2 + N_R^2) - \frac{i}{\gamma\tau_r}\kappa^2 = 0. \quad (136)$$

Thermal relaxation and thermal diffusion should mimic the limits of cooling in optically thin and in the optically thick regimes. The difference is that thermal relaxation happens at all scales at the same time, as expected if photons are simply allowed to escape. The mode is therefore ballistic, with all scales of the disk executing the same oscillation (in the local box only; in a global disk the epicyclic frequency is a function of radius and height). The growth rate is

$$\sigma = -\frac{1}{2} \left[\frac{\mu^2 \beta N_R^2}{\beta^2 + \mu^2 (\kappa^2 + N_R^2)} \right] \quad (137)$$

where $\beta = 1/\gamma\tau$ is the inverse of the cooling time and $\mu = k_z/k$, with k_z the vertical wavenumber, and $k^2 = k_R^2 + k_z^2$, where k_R is the radial wavenumber.

The most unstable cooling time is

$$\tau_{\max} = \frac{1}{\gamma} \left| \frac{k}{k_z} \right| \frac{1}{\sqrt{\kappa^2 + N_R^2}} \quad (138)$$

with associated growth rate

$$\sigma_{\max} = -\frac{1}{4} \left| \frac{k_z}{k} \right| \frac{N_R^2}{\sqrt{\kappa^2 + N_R^2}} \quad (139)$$

The fastest growth rates occur for $k_z \gg k_R$, i.e., relatively flat and radially elongated epicycles¹¹. If we also assume Keplerian disks ($\kappa = \Omega \gg |N_R|$),

$$\tau_{\max} = \frac{1}{\gamma\Omega} \quad (140)$$

$$\sigma_{\max} = -\frac{N_R^2}{4\Omega}. \quad (141)$$

Diffusion on the other hand is characterized by a random walk of photons, with a characteristic length scale set by its Laplacian scaling. Latter (2016) finds the same growth rate in the diffusion regime, now with a length-dependent cooling time $\beta = \chi k_z^2$, where χ is the thermal diffusivity. Maximum growth occurs for $\beta = \Omega$, setting the wavenumber of maximum growth $k_z = \sqrt{\chi/\Omega}$, with same growth rate as in the optically thin cooling law.

We show in Fig. 9 (left panel) the evolution of a 3D simulation of convective overstability. We set a box of size $4H \times 16H \times 2H$, with resolution $256 \times 256 \times 128$ in x , y , and z , respectively, including the linearized pressure gradient. When the initial k_z mode saturates (at 50 orbits), a sharp rise in enstrophy occurs, developing into a large scale vortex. The saturated state is identified with the SBI.

Some words are warranted about the robustness of the COV as an astrophysical process relevant to disks. The condition that $N_R^2 < 0$ requires (for negative radial pressure gradient)

$$q_\rho - \frac{q_T}{(\gamma-1)} < 0 \quad (142)$$

where q_ρ is the power law index of the density gradient and q_T the power law index of the temperature gradient. For a column density following a power law

¹¹ In the local box we could set $k_R = 0$ and obtain a channel flow. Yet, while insightful, channel flows are an artifact of local boxes, not possible in global disks where κ is a function of radius. Also, setting $k_R = 0$ violates the short wave approximation for obtaining the dispersion relation. It suffices to set $k_z \gg k_R$ to obtain the maximum growth rate. Interestingly, this contrasts with the dominant VSI mode, which is the very opposite, $k_R \gg k_z$, a tall slender mode. This should help future simulations prone to both instabilities to be able to distinguish between the processes.

$$\Sigma \propto \rho H \propto r^{-q_\Sigma} \quad (143)$$

we have for a Keplerian disk

$$q_\Sigma = q_\rho + \frac{q_T}{2} - \frac{3}{2} \quad (144)$$

The requirement of Eq. (142) is then

$$2q_\Sigma < q_T \frac{(\gamma + 1)}{(\gamma - 1)} - 3 \quad (145)$$

which, for $\gamma = 7/5$ means

$$q_\Sigma < 3 \left(q_T - \frac{1}{2} \right) \quad (146)$$

For $q_T = 1/2$ the column density has to be flat or increasing with distance in order to lead to instability, which is not reasonable. For $q_T = 3/4$ the onset of instability in the midplane corresponds to $q_\Sigma = 3/4$ (also for $\gamma = 7/5$). While this is consistent with the range of $q_\Sigma \approx [0.4, 1.0]$ found in the observations of Andrews et al. (2009), it lies in the middle of the range and thus the COV may not be robust in the midplane.

That does not mean that the COV is not present in general. The VSI does not formally exist in the midplane either, yet the unstable layers above and below are enough to drive the whole disk into a turbulent state as shown in numerical simulations. Indeed, for the COV, there exists the possibility of unstable radial entropy gradients away from the midplane, even when the midplane is stable. The entropy gradient is

$$\frac{\partial s(R, z)}{\partial \ln R} = \frac{\partial \ln T(R, z)}{\partial \ln R} - (\gamma - 1) \frac{\partial \ln \rho(R, z)}{\partial \ln R} \quad (147)$$

which, for the isothermal stratification given by Eq. (21), becomes

$$\frac{\partial s(r, Z)}{\partial \ln R} = -q_T + (\gamma - 1) \left[q_\rho - \frac{z^2}{2H^2} (3 - q_T) \right] \quad (148)$$

For the MMSN model (Hayashi 1981), with $q_T = 0.5$ and $q_\Sigma = 1.5$, then for $\gamma = 1.4$ the entropy gradient, which is 0.6 at the midplane, flips sign and becomes negative at $z = \sqrt{1.2}H \sim H$. Whether this is near the midplane enough to render the whole disk column turbulent remains to be shown by numerical simulations.

Notice also that yet another entropy gradient is to be considered for the nonlinear sibling of the COV, the SBI. Being essentially a vertically global COV with $k_z = 0$, the relevant quantities to be checked for radial buoyancy are the column density gradient, and the vertically integrated pressure and entropy. In this case, the vertical integration of the polytropic equation of state passes from $p \propto \rho^{1+1/n}$ to $P \propto \Sigma^{1+1/\tilde{n}}$, with (Goldreich et al. 1986)

$$\tilde{n} = n + 1/2 \quad (149)$$

which is equivalent to an effective adiabatic index

$$\tilde{\gamma} = \frac{3\gamma - 1}{\gamma + 1}. \quad (150)$$

and the condition of $N^2 < 0$ now becomes simply $q_T = (\tilde{\gamma} - 1)q_\Sigma$. We overplot in Fig. 10 densities and temperature gradients for a sample of disks from Andrews & Williams (2007). According to this criterion we see that most disks in the sample should be susceptible to the SBI.

Finally, we caution that although the COV exists in the local box, its existence has not yet been established in global disks. The different between these models is tied to what we just discussed previously. In a global disk the entropy gradient is allowed to adjust to the flow, whereas in the local box it is hardcoded and enforced. Global simulations of the COV would be useful to resolve the issue. If the thermal diffusion is set by the turbulence itself, with $\chi = \alpha \Omega H^2$, then the maximally growing wavelength of the instability is $\sqrt{\alpha}H$, or roughly $0.07H$. For $H/R = 0.05 - 0.1$, between 1500 and 3000 points in the radial direction are needed to resolve the instability in global models.

4.4.3. Finite Amplitude Initiated Turbulence: the Zombie Vortex Instability

Prior to the discovery that the MRI is a viable process to drive turbulence in protoplanetary disks, researchers long struggled (in vain) to identify a purely hydrodynamic *supercritical* route to turbulence. During the heyday of the MRI, many adherents of the hydrodynamic route began examining the possibility that a *subcritical* turbulence transition may be possible in protoplanetary disks (Balbus 2003). In this picture it is argued that while a Keplerian disk initiated with a low-amplitude velocity field should quickly shear away incipient shear driven dynamic activity, a relatively long-lived turbulent state could take root if the initial flow field were either of sufficiently high-amplitude (i.e., with speeds approximately that of the local c_s) or seeded with perturbations that result in strong transient growth which might trigger could trigger a secondary transition in the flow (Chagelishvili et al. 2003; Yecko 2004).¹²

Richard & Zahn (1999) examined the earliest Taylor-Couette experiments – those of Wendt’s 1933 experiments report and repeated by G.I. Taylor (Taylor 1936) – that are both stable to the Taylor-Couette instability and support a flow profile exhibiting an increase of angular momentum with axial distance. Interpreting this as reasonably mimicking a Keplerian flow and extrapolating the measured laboratory torques (and corresponding effective turbulent viscosity) onto flows with the astronomical values of Re appropriate to protoplanetary disks, they argue that such disks should easily support a turbulent state owing to their small viscosities even with the smallest of initial triggers. Follow-up laboratory work to test this proposition has been inconclusive with contradictory results reported (Ji et al. 2006; Pao-

¹² The idea of transient growth is that certain small amplitude perturbations can result in large amplitude fluctuations in the perturbation energy in a strongly sheared flow. This notion has been shown to explain the transition to turbulence in viscous three-dimensional flows which are otherwise linearly stable (Butler & Farrell 1992). For Keplerian disks, the amplification factor in the perturbation energy, given by G_{\max} , was shown in Yecko (2004) and Maretzke et al. (2014) to have a $Re^{2/3}$ dependence. For a comprehensive review of the ideas of transient growth in strongly sheared flows see Schmid & Henningson (2001).

letti et al. 2012) and theoretical analysis of the laboratory setting identify the source of instability as emanating from the axial boundaries of the experiment causing the laboratory measured outward transport of angular momentum (Avila 2012). Subsequent higher Re laboratory studies (Edlund & Ji 2014, 2015) and numerical experiment (Lopez & Avila 2017) has shown that the observed turbulence increasingly recedes and becomes localized to the axial caps of the system and is entirely the result of triggered Ekman boundary layer flow phenomenon. These authors also show that as Re is increased, the flow increasingly appears laminar and self-similar within the bulk interior of chamber. The results of these efforts showcase the importance of doggedly assessing the character of these systems at increasingly higher values of Re as well as highlighting the dangers of deriving conclusions regarding the behavior of protoplanetary disks based on relatively low Re quasi-Keplerian laboratory flows and their numerical experiments (Balbus 2017).

Nevertheless, the idea that finite amplitude perturbations may play a role in the life of a protoplanetary disk has lead to the discovery of several processes that can lead to dynamically interesting end-states like the Rossby Wave Instability (Lovelace et al. 1999) and the so-called Subcritical Baroclinic Instability (Klahr & Bodenheimer 2003; Petersen et al. 2007a; Lesur & Papaloizou 2010; Lyra & Klahr 2011). Each of these processes appear to generally lead to the emergence of coherent, quasi-steady, and relatively stable vortex structures and while these are interesting in their own right – e.g., in their ability to attract and accumulate dust grains required for planet assembly – they themselves do not appear to play a role in driving hydrodynamic turbulence in the sense we envision.

The zombie vortex instability (ZVI) is a recently identified third hydrodynamical process that has the potential to initiate widespread turbulence in protoplanetary disks. Unlike the VSI and the COV, the ZVI is a finite amplitude instability. It differs from the aforementioned finite amplitude examinations in that it requires there to be a sufficiently large vorticity field as opposed to a relatively large amplitude velocity perturbation.

Its mechanism of how a vortex column or sheet can render a flow unstable and induce spreading can be rationalized in a simple model, as shown in Fig. 11, which is based on the original findings of Marcus et al. (2013). In this study, a tubular vortex filament is oriented in the azimuthal direction in a constantly vertically stratified fluid in a local shearing box setting with a locally applied Keplerian shear. Azimuthal vibrations of the vortex filament (Rossby waves) induce a response in the fluid around it with an associated frequency. At some radial distance from the filament, this Rossby wave frequency will appear Doppler shifted due to the Keplerian shear. This Doppler shifted frequency will find resonance with a buoyancy frequency at some radial distance away in the disk, amplifying the localized buoyant perturbations. The location and very narrow radial extent where this resonance operates is called a "critical layer". The amplified perturbation drives the generation of new filaments which also turn into vortices. In doing so, the newly generated filaments excite other

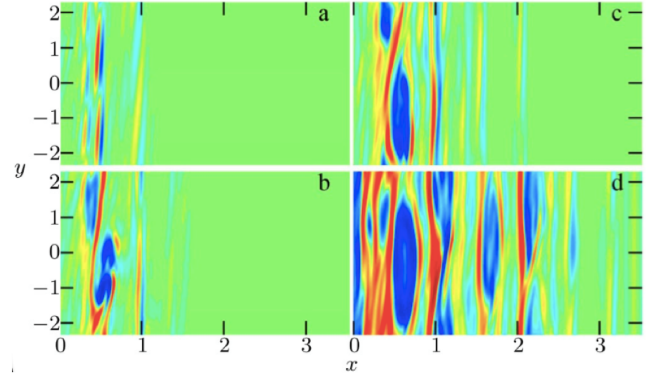


FIG. 11.— Cascade of baroclinic critical layers resulting in turbulence. Color coded is the Rossby number (gas vorticity over Keplerian vorticity) in an xy plane off the midplane ($z = 0.4\Delta$). The simulation was initialized with a vortex in the midplane, not visible at this height. The vortex layers associated with baroclinic critical layers are seen at the locations $x/\Delta = m$ for non-zero integer m . Anticyclonic vorticity is indicated by blue, while cyclonic vorticity is red; the darkest red/blue colors correspond to $Ro = \pm 0.10$, while green indicates $Ro = 0$. (a) $t = 64$ orbits, (b) $t = 256$ orbits, (c) $t = 576$ orbits, and (d) $t = 2240$ orbits. Reproduced from Marcus et al. (2013).

buoyant resonances further on and, thereby, repeating the process and setting the whole disk into a turbulent state (Marcus et al. 2013; Umurhan et al. 2016b)¹³.

There are minimum criteria for filaments to cause this kind of eruption. The first of these is that the Rossby number (Ro) of the anomalous vorticity must exceed a critical threshold. The Ro is assessed based on the velocity fluctuation, v , around the base Keplerian state \bar{v} . We are reminded that in a fluid shearing box rotating around the central star with angular frequency Ω , the Keplerian shear is $\bar{v} = -(3/2)\Omega x$, where x is the radial coordinate with respect to r_0 . If the radial extent of the filament is ℓ_0 and we take v to be the deviation azimuthal velocity characterized by some speed scale δv_0 , then an estimate for Ro is

$$Ro \equiv \left| \frac{\partial v}{\partial x} \right| / 2\Omega_0 \approx \frac{\delta v}{2\Omega_0 \ell_0}. \quad (151)$$

Typically, the nature of the filament will be identified as "cyclonic" if $\text{sgn}(\partial v / \partial x) > 0$ and "anti-cyclonic" otherwise (not including zero). Marcus et al. (2013) and Marcus et al. (2015) showed that filaments must have $Ro > Ro_c \approx 0.2$ in order for the ZVI to be initiated. However, Umurhan et al. (2016b) also showed that the ZVI may be instigated for lower values of Ro_c approaching even zero. What is important to note here is that minimum requirement for the filament's vorticity must have its $Ro > Ro_c$, so it implies that *there is no minimum perturbation velocity needed* to get the instability to go. Only the filament's vorticity matters since a radially-thin az-

¹³ The name of "zombie", a fictional undead creature resulting from the reanimation of a corpse, is given because these vortices happen in the Ohmic "dead" zones of protoplanetary disks. Because the process gives rise to new vortices by the excitation of critical layers – that in turn replicate the process – the effect reminds one of the spread of an infection. Another analogy would be that of tuning a guitar. Strike a note in a string that another string is tuned to, and the resonance will make the unstruck string vibrate. An attempt to rename the process "Guitar String Instability" will not be undertaken.

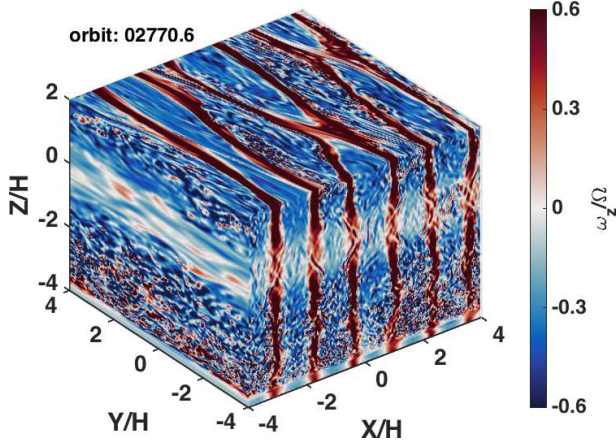


FIG. 12.— Anomalous vertical vorticity profile from fully developed ZVI simulations. Notice the banded structure in vertical vorticity, implying weak undulations atop the basic Keplerian profile. Reproduced from Barranco et al. (2018).

imutally elongated filament with velocity scale δv_0 can satisfy the minimum vorticity requirement so long as $\delta v_0/\ell_0$ remains finite as $\ell_0 \rightarrow 0$ (see also discussion in Sect. 3.3).

Because the ZVI relies on excitation of baroclinic critical layers, its growth times are relatively long once $\text{Ro} > \text{Ro}_c$, with growth rates of $< 0.05 - 0.1\Omega^{-1}$. The ZVI operates most effectively in the limit of very long cooling times as demonstrated by Lesur & Latter (2016), who examined the ZVI under a variety of thermal cooling times (whether driven by optically thin or optically thick cooling) and showed that the critical cooling time, τ_r , to be longer than 10 orbits in order for the ZVI to be dynamically significant. This corresponds to approximately a minimum gas opacity of $> 50\text{cm}^2/\text{g}$. This can be rationalized since the ZVI resonance mechanism requires buoyancy oscillations to be maintained over long timescales. For this reason, the second criterion is that the process requires the gas to be close to adiabatic, with very long cooling times.

The spawned vorticity will have an anomalous vorticity that is jet-like (Umurhan et al. 2016b), i.e., a side-by-side pair of vortex filaments of alternating signed vorticity. The radial size of this anomalous jet is the size of the critical layer and, furthermore, it is the anticyclonic part of this jet that undergoes secondary transition.

Marcus et al. (2015, 2016) showed that the ZVI leads to widespread turbulence in realistic shearing box models in which the vertical component of gravity shows the proper vertical dependence $g \sim -\Omega^2 z$. These studies show that the ZVI appears at locations away from the midplane where the stratification is strong and subsequently spreads down toward the midplane, suggesting that the process can operate even when the stratification is weak, which is consistent with predictions made in analytical work (Umurhan et al. 2016b). Marcus et al. (2016) also show that the saturated state has a turbulent spectrum $\mathcal{E} \sim k^{-5/3}$ suggesting that a downscale direct energy cascade has been resolved in these simulations (Fig. 13). We note that the starting point of the inertial spectrum appears to correspond to the critical layer scal-

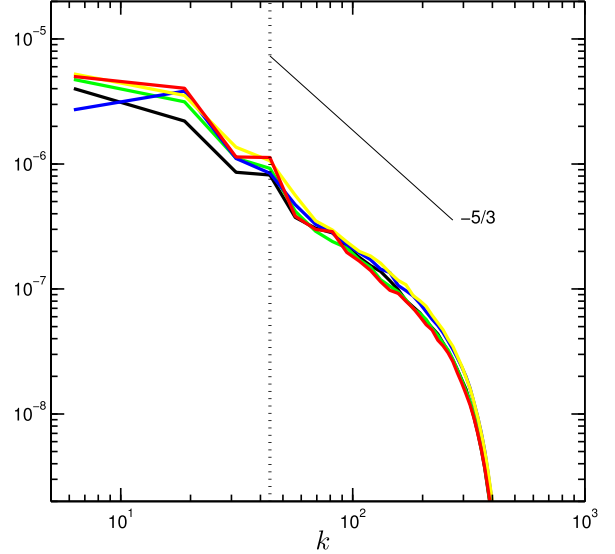


FIG. 13.— Energy spectra of the non-Keplerian component of kinetic energy in ZVI turbulence, based on simulations in the shearing box whose box size = H . The different lines represent different initial conditions: Kolmogorov noise with initial rms Mach number of 0.01 (black); Kolmogorov noise with initial rms Mach number of 0.007 (green); Kolmogorov noise with initial rms Mach number of 0.004 (blue); noise with an energy spectral index of 1.0 and initial rms Mach number of 0.007 (red); and a run initialized with an isolated anticyclonic vortex (yellow). At late-time flows are all attracted to the same energy spectrum, regardless of the initial conditions. Vertical lines correspond to scales $\approx 0.1H$ which marks the beginning of the $k^{-5/3}$ spectrum. For $80 < k < 300$, the spectra are approximately Kolmogorov. Based on reported values of $\alpha \sim 4 \times 10^{-4}$ and $h = 0.05$, a nominal value of the Rhines scale of $\lambda_b = \pi H$, based on Eq. (47), although see text for caveats. Reproduced from Marcus et al. (2016).

ing (see below). The emergence of large-scale organized zonal flows (see below) suggests that a subtle interplay of both processes may be at play.

The injection scales are those of the critical layers. Unlike in purely hydrodynamic shear flows, where the size of the critical layer is set by the viscosity of the gas and scales like $\text{Re}^{-1/3}$, the size of the critical layers (Δ_c) driving the ZVI is set by the intrinsic linear growth rate σ with an approximate scaling given by $\Delta_c \approx \sqrt{N/\Omega} \cdot \sqrt{\sigma/\Omega} k_z^{-1}$ where k_z is the vertical wavenumber of the fastest growing mode expressed in inverse units of H (Umurhan et al. 2016b). As the growth rate depends upon the vorticity of the triggering filament and the Brunt-Väisälä frequency, it is difficult to assess generalized expected length scale for Δ . Results of published simulations, together with these analytical considerations, suggest that $\Delta_c \sim 0.1H$ or less.

Lesur & Latter (2016) also find that the saturated state of the ZVI is similar to that of the COV and VSI, with anticyclonic vortices and cyclonic sheets in the largest scales. These authors conclude that the small scales appear characterized by more isotropic turbulence. Barranco et al. (2018) examine similar behavior but they also show something quite remarkable. They show that long-time simulations of the ZVI leads to the emergence of large scale, axisymmetric, radially periodic zonal flow. Each successive zonal flow sheet exhibits periodic cyclonic and anti-cyclonic behavior with a ra-

dial wavelength of about 1 scale height. Moreover, this periodic flow exhibits *temporal intermittency* in which the anti-cyclonic portion of the zonal flow periodically breaks-down after 50-100 orbit times, but eventually the flow reorganizes into the zonal flow again – presumably driven by the small scale ZVI itself (Fig. 14). Might this be an indication of an inverse cascade of energy and its transfer onto large scale zonal flows as might be expected by the Rhines mechanism? This remains to be fully explored.

Is this to be expected for protoplanetary disks? As we stated in the introduction of this section, the ZVI is not a linear instability in the usual sense, but rather a finite-amplitude process. It requires a seed vortex filament (or a spatially distributed spectrum) to launch the process with the vorticity of the filament being an order 1 fraction of the Keplerian flow itself. Generating such an initial finite amplitude state in order to spawn the ZVI cascade/spread was raised by Umurhan et al. (2016b) and Lesur & Latter (2016) as a concern that limits the applicability of the ZVI in actual disks. Marcus et al. (2016) address this matter stating an initial flow state structured with an energy spectrum $\sim k^{-a}$, with $1 < a < 3$, will always support a small scale exhibiting anomalous vorticity satisfying the minimum requirement. For example, following our discussion in Sect. 3.2, a Kolmogorov spectrum ($a = 5/3$) has an anomalous velocity $\delta v \sim \epsilon^{1/3} k^{-1/3}$. Its corresponding vorticity scale would be $\omega \sim \delta v / \ell = \delta v \cdot k \sim \epsilon^{1/3} k^{2/3}$. Thus, even for a weak initial Kolmogorov energy spectrum $\mathcal{E}_0(k)$, – whose total integrated energy is controlled by $\epsilon^{1/3}$ – there always exists a large enough value of k_0 in which ω_0 satisfies the minimum criterion – provided, of course, $k_0 < k_{diss} = 2\pi / \ell_{diss}$.¹⁴

Whether or not this process can be self-sustaining and lead to a turbulent state under a wide umbrella of conditions appropriate to the Ohmic zone remains to be determined. It would seem that its self-sustainability depends centrally on what way the original disturbances are structured and how they arrive. Although Marcus et al. (2016) find that the critical finite amplitude in the velocity field to be very small ($Ma \approx 10^{-6}$), sustaining a coherent perturbation for long enough times may still be of concern. However keeping in mind the foregoing discussion, the minimum velocity scale quoted in Marcus et al. (2016) is a value inferred based on the limited resolution of their simulations and is probably indicative of a maximum lower limit because higher resolved simulations would permit the introduction of radially narrower filaments that both satisfy the requisite anomalous vorticity criterion while exhibiting even smaller values of Ma . Also, Lesur & Latter (2016) and Marcus and co-workers find the instability numerically when hyperdiffusion is used - hyperdiffusion is an instance of Large Eddy Simulation (LES, see further below). When Laplacian viscosity is used, Lesur & Latter (2016) find that the Reynolds numbers must significantly exceed 10^7 in order for the process to lead to sustained disorga-

¹⁴ We note that a spectrum of the sort envisioned contains disturbances of every shape for any given value of k . It is that part of the flow field that gives rise to filaments with little azimuthal structure that would trigger the instability.

nized activity. While the Re for disks easily satisfies this criterion, it still remains to be understood how the resonance mechanism can sustainably extract energy from the critical layer and what might be the overall structure of the disk after ZVI turbulence has acted on it.

Where might the ZVI be active? There are several locations in the disk that, if seeded with suitable initial vorticity field, may erupt into ZVI turbulence (see further in Sect. 5). Another idea we conjecture is that ZVI may emerge perhaps near the boundary of magnetically active regions or near disk zones with pressure bumps, i.e., locations that can support radially localized Rossby waves. For example, simulations of protoplanetary disks indicate that strong zonal flow features appear at the boundary separating MHD active zones from purely hydrodynamic zones (Varnière & Tagger 2006; Lyra & Mac Low 2012; Lyra et al. 2015). Such zonal flows support Rossby waves. Since the ZVI mechanism requires there to be a Rossby wave to resonate with a buoyancy oscillation somewhere in the hydrodynamic regions of the fluid, the zonal flow characterizing this transition region might act like a large amplitude loud-speaker by providing the energy – in the form of the parent Rossby wave – to set off the eruption that could lead to ZVI turbulence spreading deep into the Ohmic zone of the disk.

5. SYNTHESIS : A BUTCHER DIAGRAM FOR HYDRO INSTABILITIES

The three hydrodynamical instabilities operate optimally in different cooling times, thus existing in very different regimes of opacity. In the adiabatic case ($\Omega\tau \gg 1$) the ZVI dominates. In the isothermal case ($\Omega\tau \ll 1$), the VSI dominates. In between these extrema, the COV operates ($\Omega\tau \sim 1$).

For what material conditions do these cooling constraints correspond? Reviewing the expression for the optically thick limit for thermal relaxation, i.e., the $\ell_{rad} \ll \ell$ expression of Eq. (129), it is evident that it depends upon the effective material opacities, density, temperature and length scale of perturbation, ℓ . Nelson et al. (2013b) examined cooling times to assess these conditions assuming values of $\ell \sim 0.1H$ (being typical of the fastest growing mode of the VSI) together with values of the expected midplane densities and radial temperature profiles based on the canonical flared minimum mass solar nebula disk models of Chiang & Goldreich (1997). Such disk models predict midplane densities and radial temperature profiles that are

$$\rho_{mid} \approx 2.7 \times 10^{-9} F(R/AU)^{-39/14} \text{ g/cm}^3, \quad (152)$$

$$T = 120(R/AU)^{-3/7} \text{ K}, \quad (153)$$

respectively, where F is the relative mass of the disk in units of minimum solar mass models. The corresponding cooling times are

$$\Omega\tau/2\pi = 168F^2 \left(\frac{\kappa_R}{\text{cm}^2/\text{g}} \right) \left(\frac{\ell}{R} \right)^2 \left(\frac{R}{20AU} \right)^{-53/14}. \quad (154)$$

The onset of the VSI for regions at around 10 AU around a $1 M_\odot$ star with $F = 1$ requires opacities of

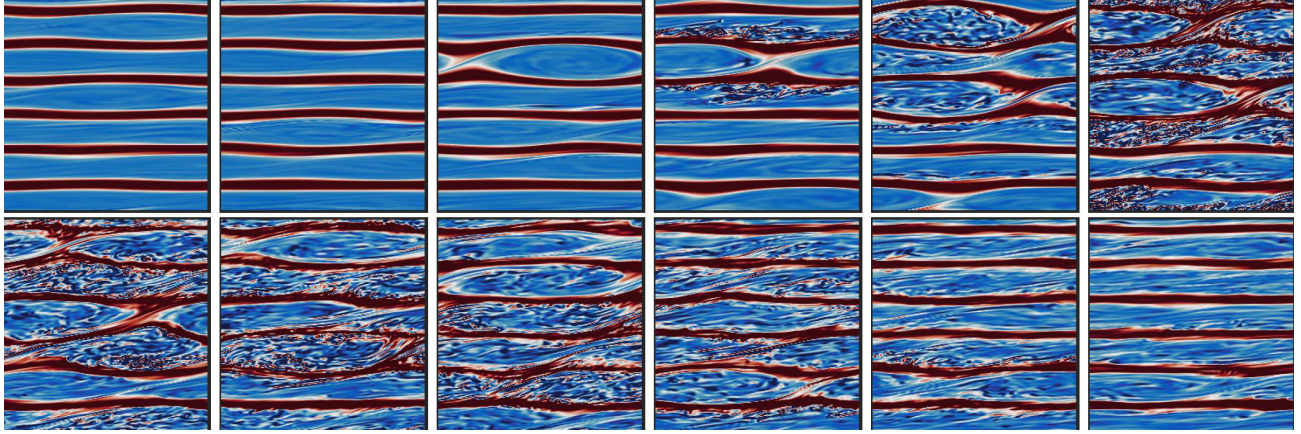


FIG. 14.— ZVI burst cycle shown as radial-azimuthal cuts at 2 scale heights of the anomalous vertical vorticity. Each successive panel corresponds to 3.5 orbit times. Banded structure undergoes a breakdown, triggering critical layer excitations along the way. Banded structure restored after 100 orbit times. Complete cycle is approximately 100 orbit times. Reproduced from Barranco et al. (2018).

TABLE 2
HYDRODYNAMICAL INSTABILITIES SUMMARY CHARACTERISTICS.

Instability	Violation of Rayleigh criterion	Mechanism Type	Linear growth rate	Length scale of linear growth	Opacity κ (cm^2/g)	Thermal time ($\Omega\tau$)	α
Vertical Shear	$d\Omega/dz \neq 0$	Angular momentum exchange between adjacent elements.	$\sqrt{m} q h\Omega/4$	$\pi q hH$	< 1	$\ll 1$	$10^{-4} - 10^{-3}$
Convective	$N_R^2 < 0$	Buoyant amplification of epicyclic oscillations.	$ N^2 /4\Omega$	$\sqrt{\chi/\Omega}$	1–50	~ 1	$10^{-4} - 10^{-3}$
Zombie Vortex	$N_z^2 > 0$	Resonance between Rossby and buoyancy frequency.	–	–	> 50	$\gg 1$	$10^{-4} - 10^{-3}$

$\kappa < 1\text{cm}^2/\text{g}$.¹⁵ Since the ZVI also has growth on similar scales the corresponding requirements suggest $\kappa > 50\text{cm}^2/\text{g}$ for the ZVI to be minimally operative. Even though the COV operates at larger scales, a reasonable estimate of the opacity is $1 < \kappa < 50\text{cm}^2/\text{g}$.

The cooling time requirement means that the ZVI will be more important in the very inner disk (inwards of 1 AU), **where the gas** is more adiabatic; the COV in the region 1-10 AU; and the VSI in the outer disk beyond 10 AU which tends to be more isothermal. As we go further outwards, the very outer disk beyond 100 AU starts to become too optically thin and the cooling time goes up again, being unstable to COV. Eventually, if the disk is too optically thin and the cooling time long enough, the disk will be unstable to ZVI. That invites a mapping of instabilities that we call a “butcher diagram”¹⁶, in Fig. 15.

The actual mapping of the instabilities depends on translating gas densities, dust densities, and temperatures, to opacities and thence to optical thicknesses and cooling times. As such, it will depend heavily on the underlying disk model assumed. The specific map shown in Fig. 15 is taken from Malugin et al. (2017), and uses the axisymmetric disk model of Hartmann et al. (1998),

also used in Dzyurkevich et al. (2013),

$$\Sigma = \Sigma_c \left(\frac{r}{r_c}\right)^{-q_\Sigma} \exp\left[-\left(\frac{r}{r_c}\right)^{2-q_\Sigma}\right] \quad (155)$$

with

$$\Sigma_c = (2 - q_\Sigma) \frac{M_{\text{disk}}}{2\pi r_c^2} \quad (156)$$

The stellar mass is $M_\star = 1M_\odot$, the reference column density is $\Sigma_c = 1700 \text{ g cm}^{-2}$ and the power law is taken as the median of Andrews et al. (2009), $q_\Sigma = 0.9$. The cutoff radius is $r_c = 40 \text{ AU}$. This profile yields a good match to both CO and continuum observations (Hughes et al. 2008), and matches the minimum mass solar nebula up to 100 AU. The temperature chosen is that of a passive disk (Chiang & Goldreich 1997)

$$T = T_0 \left(\frac{1\text{AU}}{R}\right)^{1/2} \quad (157)$$

with $T_0 = 280 \text{ K}$. Vertical temperature gradients are ignored, and a lower limit of 10 K set beyond 250 AU. Using the dust opacities from Semenov et al. (2003) and a well-mixed dust at the dust-to-gas ratio of 10^{-2} , one obtains the mapping in Fig. 15 for the appropriate cooling times described in the text. Ignoring vertical temperature gradients is valid for passive-disks (Chiang &

¹⁵ Note that the opacity is the effective opacity of a fluid mixture of gas and dust. Typically minimum mass solar nebula models assume a 1 percent content of dust grains.

¹⁶ Inspired by diagrams delineating various cuts of beef.

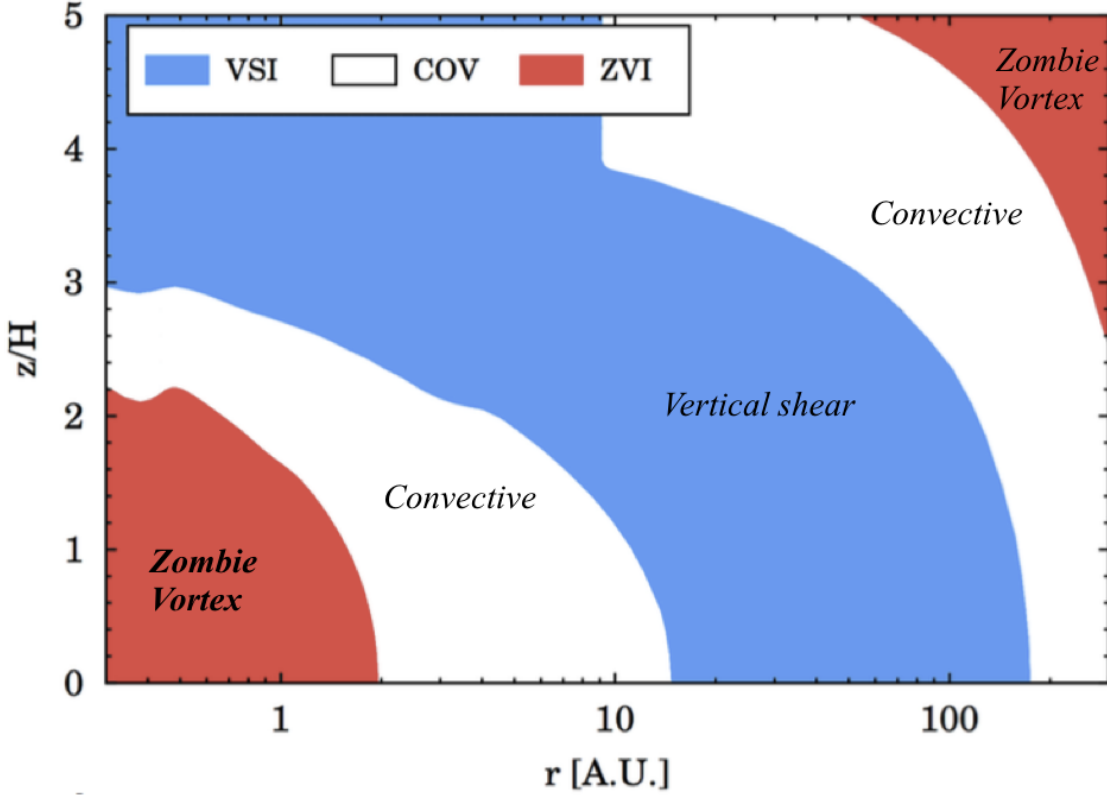


FIG. 15.— A “butcher diagram” for hydrodynamical instabilities. Disk opacities define cooling times that, in turn, determine which hydrodynamical instability process is dominant. The ZVI dominates for long cooling times, happening at the optically thick inner disk. The COV requires moderate cooling times, happening in the 10 AU region. The VSI happens where the disk is more isothermal. As one moves outwards, the disk becomes more optically thin and thus the cooling time increases again, leading to a new zone of COV and eventually another adiabatic region for the ZVI. The regions where ZVI dominate may be too ionized and thus prone to MRI (in the inner disk) or magnetocentrifugal winds. Adapted from Malygin et al. (2017). The different instabilities have different saturation mechanisms: the VSI saturates via RWI, the COV via SBI, and the ZVI via itself and RWI.

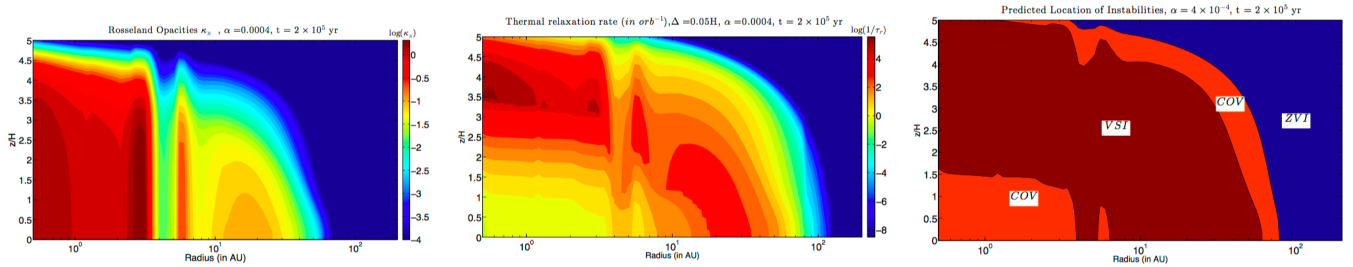


FIG. 16.— Thermal properties of global alpha-disk models. Left: Rosseland mean opacities after 2×10^5 yr. Opacities quoted in units of cm^2/g . Middle: Derived thermal relaxation times after 2×10^5 yr. Cooling time τ in unit of local orbit times around a $1 M_{\odot}$ star. Right: A butcher diagram indicating locations where various instabilities are operating based on output of Estrada et al. (2016): 2×10^5 years, $\alpha = 4 \times 10^{-4}$ and dust porosities of zero. Adapted from Umurhan et al. (2017).

Goldreich 1997). However, disks in which there is some amount of viscous heating will show potentially strong deviations from nearly uniform and this is expected to be the case if the turbulence is relatively strong $\alpha > 10^{-2}$ like, for example, the global disk evolution models considered in Bitsch et al. (2015). For the kinds of hydrodynamic instabilities discussed here, wherein $\alpha < 10^{-3}$, viscous heating is expected to be a secondary effect.

Using the coagulation/fragmentation and dust evolution model of Estrada et al. (2016), and assuming equal

Rosseland mean and Planck mean opacities, the temperature profiles are largely locally isothermal (with mid-plane to lid-temperature variations of less than 1 K). The radial temperature dependence is given by $T \sim R^{-3/7}$ for disk radii > 3 AU, typical of flared disks and consistent with theoretical predictions (Chiang & Goldreich 1997). Umurhan et al. (2017) displays the effective dust opacities in a disk experiencing some amount of alpha-disk turbulence according to the disk evolution model of Estrada et al. (2016). The model compiled distributes

dust particles in vertical height according to the turbulent intensity ($\alpha \sim 4 \times 10^{-4}$) and the dust size which together yield a turbulent Stokes number. Estrada et al. (2016) determine the size of particles as a function of disk radius and epoch. The left panel of Fig. 16 shows a profile of the internal opacities at a model after $t = 2 \times 10^5$ years of dust evolution. The thermal relaxation times can be very roughly represented as either dominated by radiative diffusion (optically thick) or radiative cooling (optically thin) regimes and are given by Eq. (129). For optically thick conditions, the middle panel of Fig. 16 shows τ for fluid structures with scales $\ell = 0.05H$, typical of the VSI. The right panel of Fig. 16 displays a butcher diagram of the instabilities considering these thermal relaxation times. The VSI dominates the turbulence in the range 3-90 AU while the COV occurs generally in the inner disk (<3 AU). The ZVI is prominent in outer solar nebula (>100 AU). This particular combination of gas and dust model never becomes optically thick enough for the ZVI in the inner disk.

We stress that at the time of this review no model combining all the three (or even two) of the instabilities has been attempted. Therefore, the boundaries between the instabilities in the butcher diagram are ill-defined. As long as the entropy gradient is negative, the COV has the least stringent thermal constraints, effectively existing for all finite cooling times. The VSI, on the other hand, seems to be the most robust in respect to the violation of the Solberg-Høiland criterion, as stellar irradiation should always enforce some amount of vertical shear. The ZVI seems to be less robust, as it requires a “prime mover” in the form of a sufficiently large finite-amplitude disturbances to be emplaced inside the dead zone. However, we conjecture that this initial finite-amplitude perturbation should be present in the RWI-unstable transition between the MRI zone and the Ohmic zone in the inner disk, where the thermal conditions are also adiabatic. We note, although, that the ZVI, being present in more adiabatic conditions, will probably be self-regulated at small α values. At the high densities of the optically thick depths of the disk, modest amounts of accretional stresses, perhaps as little as $\alpha \sim 10^{-5}$ are sufficient to generate enough heat to bring the stratification to a profile that shuts down the ZVI. Table 2 summarizes the parameters of the instabilities.

6. NEAR FUTURE GOALS FOR NUMERICAL SIMULATIONS OF DISK TURBULENCE

The near and long term goals of numerical modeling of turbulence in the protoplanetary disk is to establish the conditions on which dust particles grow into planetesimals on a 0.5Ma to 2.3Ma time frame after the appearance of Calcium Aluminium Inclusions (CAI’s). This means properly characterizing the turbulent velocity field on scales where the dust particles accumulate. From our standpoint it is incumbent on the fluid dynamicists and theorists to establish, with some confidence, the quality of the energy spectrum at the relevant scales and the first step toward this is identifying and quantifying the shape of the turbulent energy spectrum in the inertial regime. If the resulting turbulent state is both steady and the turbulence in the iner-

tial range is indeed self-similar, then upon its resolution the inertial spectrum could be extrapolated down to the smaller scales where dust collection is thought to be actively taking place.

A case that illustrates the path forward is the state of our understanding of the VSI. Simulations conducted thus far have been only moderately resolved. For example, in the original simulations conducted by Nelson et al. (2013b) where the radial domain was a radial annulus from $R = R_0$ to $R = 2R_0$, the conditions of the disk were such that the fastest growing mode had a wavelength of $\ell_0 = 0.008R_0$. Note that on these scales, the pressure scale height is $\sim 0.05R_0$. These simulations resolved this fastest growing mode with about 15 grid points. With ℓ_0 being nominally the injection scale, in order to begin seeing the emergence of an inertial regime requires at least 10-100 times the resolution achieved in those simulations. For the kinds of global scale simulations currently feasible, such high resolution studies is still quite prohibitive.

One way around this is to consider very narrow global simulations or appeal to the often maligned shearing box setting (Goldreich & Lynden-Bell 1965; Umurhan & Regev 2004; Latter & Papaloizou 2017), which represents a model facsimile of a box section of a disk orbiting the central star at the reference radius $R = R_0$. The spatial scales of the box are usually in units of the local scale height so, in principle, higher resolution simulations are possible. For example, simulations of the ZVI are performed in this model setup and, as the results of Marcus et al. (2016) shows, they were able to resolve a Kolmogorov like spectrum. In the context of the VSI, for example, adjustments to the formulation of the shearing box equations that are suitable for the mechanism may be needed, like the composite local-global model suggested by McNally & Pessah (2015). If a shearing box model is used then the global scale variations that give rise to each of the three instabilities must be carefully represented within the confines of these models. For example, the global scale variation of the temperature field must be faithfully represented on the small scales in just the right way so that the instability is triggered. Careful thought must also be given to the choice of boundary conditions adopted, making sure that they do not contaminate the results obtained.

Because the molecular viscosity of H_2 is so small, it is practically impossible at this time to conduct direct numerical simulations (DNS) that resolve the flow down to the dissipation scales. Since energy cascades toward small scales in fully turbulent supercritical 3D flows¹⁷, unless the natural dissipation scales are resolved in flow modeling, then power can build up at the grid scales of a simulation leading to unrealistic and, often times, numerically unstable situations. Large Eddy Simulation (LES, Davidson (2004)) is one way to confront this problem. An LES simulation will introduce a high order diffusion operator, like $\nu_4 \nabla^4$ or $\nu_8 \nabla^8$ or even $\nu_{16} \nabla^{16}$, into the equations of momentum conservation. The overall strength of the dissipation is controlled by the “hyperdiffusion” coefficient ν_n , where n is the order of the Laplacian operator. With a suitably chosen value of the

¹⁷ ...and if 2D flow, then enstrophy cascades toward small scales.

coefficient ν_n a hyperdiffusion operator permits the normal cascade of energy through the inertial regime of a turbulent flow but will increasingly dissipate power as the grid scales are approached in a simulation. This is intended to mimic the continued transference of power to the unresolved dissipation scales by artificially dissipating the energy flux at the resolved scale of the simulation. This is usually a delicate procedure requiring careful tuning of ν_n . LES, or any other equivalent small-scale energy dissipation procedure, is an essential tool for numerical modeling of protoplanetary disk turbulence that will be necessary for the foreseeable future.

7. CONCLUSION

The past decade of disk research have seen the emergence of disk instability mechanisms that provide hydrodynamical turbulence in the Ohmic dead zone. They violate the Rayleigh criterion in different ways. The vertical shear instability (VSI) by having $d\Omega/dz \neq 0$, the convective overstability (COV) by the presence of entropy gradients with $N_R^2 < 0$, and the zombie vortex instability (ZVI) with $N_z^2 > 0$. Because of these requirements, they exist in very different regimes of opacity: the ZVI in adiabatic regions, the VSI in isothermal ones, and the COV in between. These can be mapped into different locations, depending on the particular disk model (Fig. 15 and Fig. 16). The instabilities have different turbulent responses, with α values around 10^{-3} . Their properties are summarized in Table 2.

Of the three processes, the most robust seems to be the VSI, as the unstable entropy gradients necessary for the COV are not necessarily realized in all disks, and the first perturbation necessary for the ZVI is difficult to maintain over long times. The three instabilities saturate into three-dimensional vortices. The VSI because of RWI and Kelvin-Helmholtz instability of the thin tall sheets. The COV because it builds up the finite difference perturbations that lead to subcritical baroclinic instability. The ZVI also via RWI and Kelvin-Helmholtz instability. All vortices decay due to elliptical instability in the cores (Pierrehumbert 1986; Bayly 1986; Lesur & Papaloizou 2009), that leads to a direct enstrophy cascade. In saturation, vortex strength should be defined by a balance between the saturation mechanism, that feeds the vortices (RWI for VSI/ZVI, SBI for COV), and the rate of decay via elliptic instability (Lyra 2013). Weaker vortices (of larger aspect ratio) linger for longer because the growth rates of elliptic instability decrease with vortex aspect ratio.

In this review, we have specifically used the term *Ohmic zone* instead of the traditional “dead” zone. We could have used “hydrodynamical” zone since Ohmic effects, in the sense of magnetic Reynolds numbers close to 1, are not at play. The Ohmic zone is deep into the resistive regime and any magnetic effect is irrelevant. Yet, we keep the name Ohmic for juxtaposition to the other non-ideal MHD effects: the Hall effect and ambipolar diffusion, that may be at play in very low density regions of the disk (Wardle 1999, 2007; Lesur et al. 2014). The Hall effect leads to the Hall shear instability if the magnetic field and the angular momentum vectors are aligned. Ambipolar diffusion leads to magnetocentrifugal winds, evidence for which may have been

recently discovered (Simon et al. 2016). The very high up region of the butcher diagram (Fig. 15) are probably prone to ambipolar diffusion, providing a “lid” for all instabilities; if the ionization fraction is high enough the MRI can be reactivated. The outer ZVI region may thus be completely quenched, by ambipolar diffusion or the MRI itself. The outer COV region is low density enough for ambipolar diffusion to operate. The VSI region may also operate optimally within the region where the Hall effect is the dominant source of resistivity. It remains to be shown how the instabilities here summarized behave in connection with these non-ideal terms.

The importance of characterizing the shape and quality of turbulence and its influence upon the growth of planetesimals, especially at the smallest scales, is one of the main messages of this review. While we have not delved into how the turbulence mitigates the growth of planetesimals, we have emphasized that the dynamical state of the protoplanetary disk is the fundamental canvas on which the particle growth narrative is etched. With this in mind, we conclude with another quote from the ancients, this time of Hesiod, who writes of the birth of the Earth (“Gaia”),

In the beginning there was Chaos; but then there came to be Gaia, the broad-breasted, the ever-secure seat of all immortals who dwell in the peaks of snowy Olympus.

Hesiod *Theogony* 116-118¹⁸

This vision strikes as modern as well: if one substitutes “chaos” with *turbulence* and “Gaia” with planetesimals, then we have a picture describing elements of today’s scientific paradigm of planet formation.

Acknowledgements. We thank Joe Barranco, Konstantin Batygin, Luca Biancofiore, Til Birnstiel, Omer Blaes, Axel Brandenburg, Simon Casassus, Thayne Currie, Jeff Cuzzi, Kees Dullemond, Natalia Dzyurkevich, Paul Estrada, Mario Flock, Sebastien Fromang, Oliver Gressel, Nili Harnik, Eyal Heifetz, Tobias Heinemann, Thomas Henning, Anders Johansen, Hubert Klahr, Willy Kley, Min-Kai Lin, Mordecai Mac Low, Philip Marcus, Frédéric Masset, Colin McNally, Heloïse Méhéut, Farzana Meru, Alessandro Morbidelli, Krzysztof Mizerski, Richard Nelson, Chris Ormel, Sebastián Pérez, Oded Regev, Luca Ricci, Giora Shaviv, Jake Simon, Neal Turner, Nienke van der Marel, Peggy Varnière, and Andrew Youdin, for their support and valuable scientific discussions over the years. We thank Willy Kley and Henrik Latter for permission to use their figures, and for comments on the draft. We thank the referee, Hubert Klahr, for substantial suggestions that vastly improved the quality of this review. We also appreciate comments from Hantao Ji and Andrew Youdin correcting several omissions from an earlier version of the work. We express gratitude to Professor Osman

¹⁸ Translation by Professor Osman S. Umurhan who notes that “ $\chi\alpha\omicron\sigma$ ” or “Chaos” represents not disorder in the modern sense, but a chasm or abyss, whose properties appear to be a dark, gaping space. Later in Hesiod’s account this very chasm appears to have the appropriate material “to catch fire” from Zeus’ thunderbolt.

Umurhan for help with classical period translations. We are especially indebted to James Y.-K. Cho for illuminating subtleties characterizing the nature of atmospheric turbulence.

W.L. acknowledges support of Space Telescope Sci-

ence Institute through grant HST-AR-14572 and the NASA Exoplanet Research Program through grant 16-XRP16_2-0065. O.M.U. acknowledges support from the NASA Astrophysics Theory Program through grant NNX17AK59G.

REFERENCES

- Abramowicz, M. A., Livio, M., Piran, T., & Wiita, P. J. 1984, *ApJ*, 279, 367
- Andrews, S. M., & Williams, J. P. 2007, *ApJ*, 659, 705
- Andrews, S. M., Wilner, D. J., Hughes, A. M., Qi, C., & Dullemond, C. P. 2009, *ApJ*, 700, 1502
- Ansdell, M. et al. 2018, *ApJ*, 859, 21
- Arlt, R., & Urpin, V. 2004a, *A&A*, 426, 755
- . 2004b, *A&A*, 426, 755
- Aumann, H. H. 1985, *PASP*, 97, 885
- Avila, M. 2012, *Physical Review Letters*, 108, 124501
- Bai, X.-N. 2015, *ApJ*, 798, 84
- Bai, X.-N., & Stone, J. M. 2011, *ApJ*, 736, 144
- . 2017, *ApJ*, 836, 46
- Balbus, S. A. 2003, *ARA&A*, 41, 555
- . 2017, *Journal of Fluid Mechanics*, 824, 1
- Balbus, S. A., & Hawley, J. F. 1991, *ApJ*, 376, 214
- Balbus, S. A., & Terquem, C. 2001, *ApJ*, 552, 235
- Barker, A. J., & Latter, H. N. 2015a, *MNRAS*, 450, 21
- . 2015b, *MNRAS*, 450, 21
- Barranco, J., Pei, S., & Marcus, P. 2018, *ArXiv e-prints*
- Batygin, K. 2018, *AJ*, 155, 178
- Bayly, B. J. 1986, *Physical Review Letters*, 57, 2160
- Beckwith, S. V. W., Sargent, A. L., Chini, R. S., & Guesten, R. 1990, *AJ*, 99, 924
- Benzi, W. 2000, *Space Sci. Rev.*, 92, 279
- Biancofiore, L., & Umurhan, O. M. 2018, *ArXiv e-prints*
- Bitsch, B., Johansen, A., Lambrechts, M., & Morbidelli, A. 2015, *A&A*, 575, A28
- Blaes, O. M., & Balbus, S. A. 1994, *ApJ*, 421, 163
- Boffetta, G., & Ecke, R. E. 2012, *Annual Review of Fluid Mechanics*, 44, 427
- Boffetta, G., & Musacchio, S. 2010, *Phys. Rev. E*, 82, 016307
- Brauer, F., Dullemond, C. P., Johansen, A., Henning, T., Klahr, H., & Natta, A. 2007, *A&A*, 469, 1169
- Bryan, M. L., Benneke, B., Knutson, H. A., Batygin, K., & Bowler, B. P. 2018, *Nature Astronomy*, 2, 138
- Butler, K. M., & Farrell, B. F. 1992, *Physics of Fluids A*, 4, 1637
- Cabot, W. 1996, *ApJ*, 465, 874
- Cameron, A. G. W. 1978, *Moon and Planets*, 18, 5
- Chagelishvili, G. D., Zahn, J.-P., Tevzadze, A. G., & Lominadze, J. G. 2003, *A&A*, 402, 401
- Chiang, E. I., & Goldreich, P. 1997, *ApJ*, 490, 368
- Davidson, P. A. 2004, *Turbulence: an introduction for scientists and engineers* (Oxford)
- de Val-Borro, M., Artymowicz, P., D'Angelo, G., & Peplinski, A. 2007, *A&A*, 471, 1043
- Diels, H., & Kranz, W. 1961, *Die Fragmente der Vorsokratiker*, vols. I and II. (Berlin Weidmann)
- Dubrulle, B., Morfill, G., & Sterzik, M. 1995, *Icarus*, 114, 237
- Dzyurkevich, N., Turner, N. J., Henning, T., & Kley, W. 2013, *ApJ*, 765, 114
- Edlund, E. M., & Ji, H. 2014, *Phys. Rev. E*, 89, 021004
- . 2015, *Phys. Rev. E*, 92, 043005
- Elsasser, H., & Staude, H. J. 1978, *A&A*, 70, L3
- Estrada, P. R., Cuzzi, J. N., & Morgan, D. A. 2016, *ApJ*, 818, 200
- Flock, M., Nelson, R. P., Turner, N. J., Bertrang, G. H.-M., Carrasco-González, C., Henning, T., Lyra, W., & Teague, R. 2017, *ApJ*, 850, 131
- Fricke, K. 1968, *ZAp*, 68, 317
- Frisch, U. 1995, *Turbulence* (Cambridge University Press)
- Gammie, C. F. 1996, *ApJ*, 457, 355
- Gamow, G., & Hynek, J. A. 1945, *ApJ*, 101, 249
- Garaud, P., & Lin, D. N. C. 2004, *ApJ*, 608, 1050
- Goldreich, P., Goodman, J., & Narayan, R. 1986, *MNRAS*, 221, 339
- Goldreich, P., & Lynden-Bell, D. 1965, *MNRAS*, 130, 125
- Goldreich, P., & Schubert, G. 1967, *ApJ*, 150, 571
- Goldreich, P., & Ward, W. R. 1973, *ApJ*, 183, 1051
- Goodman, J., & Xu, G. 1994, *ApJ*, 432, 213
- Gressel, O., Turner, N. J., Nelson, R. P., & McNally, C. P. 2015, *ApJ*, 801, 84
- Haghighipour, N., & Boss, A. P. 2003, *ApJ*, 583, 996
- Hartmann, L., Calvet, N., Gullbring, E., & D'Alessio, P. 1998, *ApJ*, 495, 385
- Hayashi, C. 1981, *Progress of Theoretical Physics Supplement*, 70, 35
- Heinemann, T., & Papaloizou, J. C. B. 2009, *MNRAS*, 397, 52
- . 2012, *MNRAS*, 419, 1085
- Hughes, A. M., Wilner, D. J., Qi, C., & Hogerheijde, M. R. 2008, *ApJ*, 678, 1119
- Ji, H., Burin, M., Schartman, E., & Goodman, J. 2006, *Nature*, 444, 343
- Johansen, A., Henning, T., & Klahr, H. 2006, *ApJ*, 643, 1219
- Johansen, A., Oishi, J. S., Mac Low, M.-M., Klahr, H., Henning, T., & Youdin, A. 2007, *Nature*, 448, 1022
- Johansen, A., & Youdin, A. 2007, *ApJ*, 662, 627
- Kippenhahn, R., Weigert, A., & Weiss, A. 2012, *Stellar Structure and Evolution* (Springer-Verlag)
- Klahr, H. 2004, *ApJ*, 606, 1070
- Klahr, H., & Hubbard, A. 2014, *ApJ*, 788, 21
- Klahr, H. H., & Bodenheimer, P. 2003, *ApJ*, 582, 869
- Koller, J., Li, H., & Lin, D. 2003, *ApJ*, 596, L91
- Krall, N. A., & Trivelpiece, A. W. 1973, *Principles of plasma physics*
- Kunz, M. W. 2008, *MNRAS*, 385, 1494
- Kunz, M. W., & Lesur, G. 2013, *MNRAS*, 434, 2295
- Latter, H. N. 2016, *MNRAS*, 455, 2608
- Latter, H. N., & Papaloizou, J. 2017, *MNRAS*, 472, 1432
- . 2018, *MNRAS*, 474, 3110
- Lesur, G., Kunz, M. W., & Fromang, S. 2014, *A&A*, 566, A56
- Lesur, G., & Papaloizou, J. C. B. 2009, *A&A*, 498, 1
- . 2010, *A&A*, 513, A60
- Lesur, G. R. J., & Latter, H. 2016, *MNRAS*, 462, 4549
- Li, H., Colgate, S. A., Wendroff, B., & Liska, R. 2001, *ApJ*, 551, 874
- Li, H., Finn, J. M., Lovelace, R. V. E., & Colgate, S. A. 2000, *ApJ*, 533, 1023
- Lin, D. N. C., & Papaloizou, J. 1980, *MNRAS*, 191, 37
- Lin, M.-K. 2014, *MNRAS*, 437, 575
- Lin, M.-K., & Youdin, A. N. 2015, *ApJ*, 811, 17
- Lopez, J. M., & Avila, M. 2017, *Journal of Fluid Mechanics*, 817, 21
- Lovelace, R., Li, H., Colgate, S., & Nelson, A. 1999, *ApJ*, 513, 805
- Lynden-Bell, D., & Pringle, J. E. 1974, *MNRAS*, 168, 603
- Lyra, W. 2013, in *European Physical Journal Web of Conferences*, Vol. 46, *European Physical Journal Web of Conferences*, 04003
- Lyra, W. 2014, *ApJ*, 789, 77
- Lyra, W., Johansen, A., Klahr, H., & Piskunov, N. 2009, *A&A*, 493, 1125
- Lyra, W., & Klahr, H. 2011, *A&A*, 527, A138
- Lyra, W., & Mac Low, M.-M. 2012, *ApJ*, 756, 62
- Lyra, W., Turner, N. J., & McNally, C. P. 2015, *A&A*, 574, A10
- Lyttleton, R. A. 1972, *MNRAS*, 158, 463
- Mac Low, M.-M., Norman, M. L., Konigl, A., & Wardle, M. 1995, *ApJ*, 442, 726
- Malygin, M. G., Klahr, H., Semenov, D., Henning, T., & Dullemond, C. P. 2017, *A&A*, 605, A30
- Manger, N., & Klahr, H. 2018, *MNRAS*
- Marcus, P. S., Pei, S., Jiang, C.-H., & Barranco, J. A. 2016, *ApJ*, 833, 148
- Marcus, P. S., Pei, S., Jiang, C.-H., Barranco, J. A., Hassanzadeh, P., & Lecoanet, D. 2015, *ApJ*, 808, 87
- Marcus, P. S., Pei, S., Jiang, C.-H., & Hassanzadeh, P. 2013, *Physical Review Letters*, 111, 084501
- Maretzke, S., Hof, B., & Avila, M. 2014, *Journal of Fluid Mechanics*, 742, 254
- Marino, R., Mininni, P. D., Rosenberg, D. L., & Pouquet, A. 2014, *Phys. Rev. E*, 90, 023018
- McCaughrean, M. J., & O'dell, C. R. 1996, *AJ*, 111, 1977
- McNally, C. P., & Pessah, M. E. 2015, *ApJ*, 811, 121
- Meheut, H., Casse, F., Varniere, P., & Tagger, M. 2010, *A&A*, 516, A31
- Mestel, L. 1965a, *QJRAS*, 6, 161
- . 1965b, *QJRAS*, 6, 265

- Nastrom, G. D., & Gage, K. S. 1985, *Journal of Atmospheric Sciences*, 42, 950
- Nelson, R. P., Gressel, O., & Umurhan, O. M. 2013a, *MNRAS*, 435, 2610
- . 2013b, *MNRAS*, 435, 2610
- O'dell, C. R., & Wen, Z. 1994, *ApJ*, 436, 194
- Ogilvie, G. I. 2016, *Journal of Plasma Physics*, 82, 205820301
- Paardekooper, S.-J. 2006, PhD thesis, Leiden Observatory, Leiden University, P.O. Box 9513, 2300 RA Leiden, The Netherlands
- Pandey, B. P., & Wardle, M. 2006, *MNRAS*, 371, 1014
- . 2008, *MNRAS*, 385, 2269
- Paoletti, M. S., van Gils, D. P. M., Dubrulle, B., Sun, C., Lohse, D., & Lathrop, D. P. 2012, *A&A*, 547, A64
- Pedlosky, J. 1982, *Geophysical fluid dynamics*
- Petersen, M. R., Julien, K., & Stewart, G. R. 2007a, *ApJ*, 658, 1236
- Petersen, M. R., Stewart, G. R., & Julien, K. 2007b, *ApJ*, 658, 1252
- Pierrehumbert, R. T. 1986, *Physical Review Letters*, 57, 2157
- Regev, O., Umurhan, O. M., & Yecko, P. A. 2016, *Modern Fluid Dynamics for Physics and Astrophysics* (Springer)
- Ricci, L., Robberto, M., & Soderblom, D. R. 2008, *AJ*, 136, 2136
- Richard, D., & Zahn, J.-P. 1999, *A&A*, 347, 734
- Richard, S., Nelson, R. P., & Umurhan, O. M. 2016, *MNRAS*, 456, 3571
- Rucinski, S. M. 1985, *AJ*, 90, 2321
- Safronov, V. S. 1972, *Evolution of the protoplanetary cloud and formation of the earth and planets.*
- Salmeron, R., & Wardle, M. 2005, *MNRAS*, 361, 45
- Sargent, A. I., & Beckwith, S. 1987, *ApJ*, 323, 294
- Schmid, P. J., & Henningson, D. S. 2001, *Stability and Transition in Shear Flows* (Springer), 558
- Sekiya, M. 1998, *Icarus*, 133, 298
- Semenov, D., Henning, T., Helling, C., Ilgner, M., & Sedlmayr, E. 2003, *A&A*, 410, 611
- Shakura, N. I., & Sunyaev, R. A. 1973, *A&A*, 24, 337
- Shakura, N. I., Sunyaev, R. A., & Zilitinkevich, S. S. 1978, *A&A*, 62, 179
- Sheehan, D. P., Davis, S. S., Cuzzi, J. N., & Estberg, G. N. 1999, *Icarus*, 142, 238
- Simon, J. B., Bai, X.-N., Flaherty, K. M., & Hughes, A. M. 2018, *ApJ*, 865, 10
- Simon, M. N., Pascucci, I., Edwards, S., Feng, W., Gorti, U., Hollenbach, D., Rigliaco, E., & Keane, J. T. 2016, *ApJ*, 831, 169
- Spiegel, E. A. 1957, *ApJ*, 126, 202
- Stoll, M. H. R., & Kley, W. 2014, *A&A*, 572, A77
- . 2016, *A&A*, 594, A57
- Stoll, M. H. R., Kley, W., & Picogna, G. 2017a, *A&A*, 599, L6
- Stoll, M. H. R., Picogna, G., & Kley, W. 2017b, *A&A*, 604, A28
- Strom, K. M., Strom, S. E., Edwards, S., Cabrit, S., & Skrutskie, M. F. 1989, *AJ*, 97, 1451
- Sun, Y. Q., Rotunno, R., & Zhang, F. 2017, *Journal of Atmospheric Sciences*, 74, 185
- Takata, T., & Stevenson, D. J. 1996, *Icarus*, 123, 404
- Tassoul, J.-L. 1978, *Theory of rotating stars* (Princeton)
- Taylor, G. I. 1936, *Proceedings of the Royal Society of London Series A*, 157, 546
- Tulloch, R., & Smith, K. S. 2006, *Proceedings of the National Academy of Science*, 103, 14690
- Turner, N. J., & Drake, J. F. 2009, *ApJ*, 703, 2152
- Umurhan, O. M. 2010, *A&A*, 521, A25
- Umurhan, O. M., Estrada, P. R., & Cuzzi, J. N. 2017, in *Lunar and Planetary Inst. Technical Report, Vol. 48, Lunar and Planetary Science Conference*, 2616
- Umurhan, O. M., Nelson, R. P., & Gressel, O. 2013, in *European Physical Journal Web of Conferences, Vol. 46, European Physical Journal Web of Conferences*, 03003
- Umurhan, O. M., Nelson, R. P., & Gressel, O. 2016a, *A&A*, 586, A33
- Umurhan, O. M., & Regev, O. 2004, *A&A*, 427, 855
- Umurhan, O. M., Shariff, K., & Cuzzi, J. N. 2016b, *ApJ*, 830, 95
- Urpin, V. 2003, *A&A*, 404, 397
- Urpin, V., & Brandenburg, A. 1998, *MNRAS*, 294, 399
- Vallis, G. K. 2006, *Atmospheric and Oceanic Fluid Dynamics* (Cambridge University Press), 770
- Varnière, P., & Tagger, M. 2006, *A&A*, 446, L13
- Wardle, M. 1999, *MNRAS*, 307, 849
- . 2007, *Ap&SS*, 311, 35
- Wardle, M., & Königl, A. 1993, *ApJ*, 410, 218
- Wardle, M., & Salmeron, R. 2012, *MNRAS*, 422, 2737
- Weidenschilling, S. J. 1977, *MNRAS*, 180, 57
- . 1980, *Icarus*, 44, 172
- Weidenschilling, S. J., & Cuzzi, J. N. 1993, in *Protostars and Planets III*, ed. E. H. Levy & J. I. Lunine, 1031–1060
- Yecko, P. A. 2004, *A&A*, 425, 385
- Yellin-Bergovoy, R., Heifetz, E., & Umurhan, O. M. 2017, *ArXiv e-prints*
- Youdin, A., & Johansen, A. 2007, *ApJ*, 662, 613
- Youdin, A. N., & Goodman, J. 2005, *ApJ*, 620, 459
- Youdin, A. N., & Shu, F. H. 2002, *ApJ*, 580, 494
- Young, R. M. B., & Read, P. L. 2017, *Nature Physics*, 13, 1135